Check for updates

Designing transition metal-based porous architectures for supercapacitor electrodes: a review

Feitian Ran, [iD] *[a] Meijie Hu,[a] Shulin Deng,[a] Kai Wang,[a] Wanjun Sun,[a] Hui Peng [iD] [b] and Jifei Liu*[a]

Over the past decade, transition metal (TM)-based electrodes have shown intriguing physicochemical properties and widespread applications, especially in the field of supercapacitor energy storage owing to their diverse configurations, composition, porosity, and redox reactions. As one of the most intriguing research interests, the design of porous architectures in TM-based electrode materials has been demonstrated to facilitate ion/electron transport, modulate their electronic structure, diminish strain relaxation, and realize synergistic effects of multi-metals. Herein, the recent advances in porous TM-based electrodes are summarized, focusing on their typical synthesis strategies, including template-mediated assembly, thermal decomposition strategy, chemical deposition strategy, and host–guest hybridization strategy. Simultaneously, the corresponding conversion mechanism of each synthesis strategy are reviewed, and the merits and demerits of each strategy in building porous architectures are also discussed. Subsequently, TM-based electrode materials are categorized into TM oxides, TM hydroxides, TM sulfides, TM phosphides, TM carbides, and other TM species with a detailed review of their crystalline phase, electronic structure, and microstructure evolution to tune their electrochemical energy storage capacity. Finally, the challenges and prospects of porous TM-based electrode materials are presented to guide the future development in this field.

aSchool of New Energy and Power Engineering, Lanzhou Jiaotong University, Lanzhou, 730070, China

bKey Laboratory of Eco-Functional Polymer Materials of the Ministry of Education, Key Laboratory of Polymer Materials of Gansu Province, College of Chemistry and Chemical Engineering, Northwest Normal University, Lanzhou, 730070, China

1. Introduction

In recent years, the gradual exhaustion of traditional fossil energy resources and the environmental crisis caused by excessive greenhouse gas emissions have led to an increasing global demand for renewable energy.[1] In this context, research on renewable and sustainable energy technologies has been rapidly developed to cope with the increasing depletion of

Feitian Ran received his PhD (2021) in Chemical Engineering and Technology from Harbin Institute of Technology. He is currently a Lecturer in the School of New Energy and Power Engineering at Lanzhou Jiaotong University. His current research focuses on the design and synthesis of functional materials for energy storage.

Feitian Ran

Meijie Hu is currently studying at the School of New Energy and Power Engineering at Lanzhou Jiaotong University. His current research interests include high-performance energy storage devices and their energy storage mechanisms.

Meijie Hu

conventional energy sources.[2] Emerging energy technologies such as solar, wind, and tidal energy have been thoroughly researched and implemented in real-world applications.[3] However, these technologies are dramatically affected by their uneven regional distribution and natural conditions, which cause a serious imbalance between electricity generation and consumption, resulting in the inefficiency and waste of these renewable energies. Thus, to solve these issues, the development of high-efficiency energy storage devices has been regarded as one of the significant factors to guarantee continuous and steady energy outputs from the above-mentioned energy sources. By virtue of their high energy storage capacity, quick response time, and flexible configuration, electrochemical energy storage systems, particularly supercapacitors and lithium-ion batteries, have developed as one of the most significant energy storage technologies that can be used for peak frequency management in renewable energy grids.

Compared to lithium ion batteries, supercapacitors possess numerous superior properties such as high power density, long cycle life, and fast charge–discharge, which make them play indispensable roles in the field of large-scale energy storage technology for the modulation of frequency and regulation of power loads. Moreover, they have broad application potential in the fields of miniature portable integrated electrochemical energy storage devices and wearable smart flexible devices.[33]

Comparing the energy density and power density of mainstream electrochemical energy storage devices, it can be seen that although supercapacitors can deliver a high power density, compared to secondary batteries, their energy density is lower, which significantly limits the promotion and development of supercapacitors.[38] Thus, to address this issue, researchers have made progress in the following aspects: (1) broadening the operating voltage of supercapacitors by adopting new types of electrolytes to achieve high energy density, and these electrolytes always have a higher decomposition voltage, higher ionic conductivity, and optimal ionic radius. (2) Developing highly electrochemically active materials such as redox active groups and polyvalent TM elements to realize large quantities of charge transfer through the reversible faradaic reaction, and thus increasing the energy storage capacity of supercapacitors. (3) Matching different anode materials and cathode materials for the assembly of asymmetric supercapacitors. In the improvement strategy, a representative example is hybrid supercapacitors, which are assembled with battery-type and capacitor-type electrodes. This integration model considerably inherits the advantages of each electrode material, thus endowing devices with preferred energy density based on the higher power density. Recently, the most popular research has been on assembling asymmetric supercapacitors by employing TM-based materials. To maximize the energy storage potential

Kai Wang received his PhD (2020) from the School of Environment and Energy, South China University of Technology (SCUT). He is currently a Lecturer in the School of New Energy and Power Engineering at Lanzhou Jiaotong University. His current research interest focuses on the design and synthesis of electrocatalysts for fuel cells, batteries and electrochemical water splitting.

Kai Wang

Hui Peng received his PhD from Northwest Normal University in 2016. He is currently a Yunting Youth Professor at Northwest Normal University. His research interests focus on electrochemical energy materials and hydrogel materials. He has published 80+ papers as the first author/corresponding author in the peer-reviewed journals including Energy Storage Materials, Small, and Chemical Engineering Journal.

Hui Peng

Wanjun Sun received his PhD (2022) from College of Chemistry and Chemical Engineering of Lanzhou University. He is currently a Lecturer in the School of New Energy and Power Engineering at Lanzhou Jiaotong University. His current research focuses on the design and synthesis of porphyrin-based heterogeneous catalysts for photocatalytic water splitting and CO_2 reduction.

Wanjun Sun

Jifei Liu received his PhD (2019) in materialogy from Lanzhou University of Technology. He is currently a Lecturer in the School of New Energy and Power Engineering at Lanzhou Jiaotong University. His research focuses on new energy materials and devices.

Jifei Liu

of TM-based electrodes, the design of controllable porous structures has become an essential means to improve the overall energy storage performance of supercapacitors.

As one of most effective approaches to control the electrode structure, designing porous architectures not only can endow TM-based electrodes with efficient ion transport pathways and high surface/interfacial area, but also modulate their electronic structure and diminish strain relaxation. When applied as supercapacitor electrodes, they can considerably shorten the ion diffusion distance, accelerate the charge transport, expose more active sites, and provide greater contact area for electrolyte ions. These interesting findings constantly advance the research on TM-based electrodes, making them a popular subject for research in the supercapacitor energy storage field. Porous TM-based electrodes are typically characterized by their porous features, which are always accompanied by substantial surface areas, high pore size distribution, and modulated porosity. These characteristics integrate the superiorities of TM such as unique d electron configurations, multiple valence states, high redox activities, and synergistic effect of multimetal atoms, thus successfully enhancing the energy density of supercapacitors.[6] Several techniques have been widely used to construct porous TM-based materials. Typically, porous TM-based electrodes can be prepared using the template strategy, such as self-templating and sacrificial templating, but the multiple steps required for removing the templates are not conducive to large-scale mass production. In addition, the growth at the epitaxial level of nanostructures on different substrates can also lead to porous structures, e.g., gaps between nanostructures under thermal transition. Chemical deposition to construct porous TM-based electrodes is also an effective strategy, which can be divided into chemical vapor deposition and electrochemical deposition. The most controllable strategy for the preparation of porous structures is the use of the intrinsic pores in the precursor, enabling the porous TM to maintain the porous morphology of the precursor after thermal conversion. Therefore, the rational design of the synthetic route will directly determine the porous architectures of TM-based electrodes, and therefore impact the improvement in the electrochemical performance of supercapacitors.

To date, porous TM-based electrodes for supercapacitors have been intensively studied, and several of the published reviews have mainly focused on the charge storage mechanism, dimension, microstructure, and phase engineering of different TM-based electrodes. However, porous architectures, as another important characteristic of TM-based electrodes, can not only endow TM-based electrode materials with efficient ion transport pathways and high surface/interfacial areas, but also modulate their electronic structure and reduce the strain relaxation. When used in supercapacitors, porous structures can accelerate the ion diffusion and electron transport, expose more active sites, and increase the electrochemical reaction kinetics of the electrodes. Considering this, a comprehensive summary concerning the design and construction of porous architectures in TM-based supercapacitor electrodes is imperative to help understand the fundamental factors that affect the charge storage process, thus guiding future research. Herein,

the recent advances in porous TM-based electrodes are summarized, mainly focusing on the typical synthesis strategies including template-mediated assembly, thermal decomposition strategy, chemical deposition strategy, and host–guest hybridization strategy. Simultaneously, the corresponding conversion mechanism of each synthesis strategy is reviewed, and the merits and demerits of each strategy in building porous architectures are also discussed. Subsequently, the TM-based electrode materials are categorized into TM oxides, TM hydroxides, TM sulfides, TM phosphides, TM carbides, and other TM species with a detailed review of their crystalline phase, electronic structure, and microstructure evolution to tune their electrochemical energy storage capacity. Finally, the challenges and prospects of porous TM-based materials are presented to guide the future development in this field.

2. Synthetic strategies and conversion mechanisms

Various advanced preparation strategies have been exploited to synthesize TM-based porous architectures for supercapacitor electrodes. The pore structure model of each TM-based product always depends to a considerable degree on to the rational design of its synthetic routes. In this section, we review and discuss the synthetic processes and conversion mechanisms of typical synthetic strategies for TM-based electrodes, mainly including template-mediated assembly, thermal conversion strategy, chemical deposition, and guest–host hybridization strategy. This study pays special attention to a deep understanding of the relationship between structural/crystalline phase transitions and electrochemical energy storage performance in TM-based electrodes.

2.1 Template-mediated assembly

Template-mediated assembly procedures usually employ either self-templates or sacrificial templates, and the synthesis of materials with porous architectures can be accomplished in several phases.[40] One prominent benefit of template-mediated approaches is their ability to precisely regulate the dimensions and configuration of the porous structure through the utilization of diverse templates and modification of the layer program.[41] Moreover, the efficient construction and customization of the porous TM-based electrode composition and porous structure can be achieved through the incorporation of co-templates or other functional atoms. Considering their conspicuous influence on the electron/ion transfer process, it is critical to fabricate TM-based electrodes with controllable organization, micro-morphology, chemical composition, crystalline phase, and interfacial stability to ensure the superior energy storage performance of supercapacitosr.[42] The template-mediated assembly strategies can be divided into two categories, i.e., self-template assembly and sacrificial template strategies, according to the attributes of the employed templates.

2.1.1 Self-template assembly. Self-templating assembly strategies include specific organic/inorganic hybridization

compositions, reactive precursors, and highly tunable synthetic processes. The solvent-based self-template assembly routine has been widely used to synthesize porous TM-based electrodes with controllable micro-morphologies, porous architectures, and pore size distributions.[43] The key to the self-templating strategy is the formation of pores and defects in the precursor crystals, which can be categorized into three types according to how they are formed, *i.e.*, selective etching, outward diffusion, and non-uniform shrinkage. By exploiting the disparity in chemical stability between the interior and exterior of the precursor crystals, selective etching creates pores through the selective etching of the templates. This method typically maintains the dimension and porous structure of the templates.[44] In the context of outward diffusion, the migration of the internal material to the external region results in the formation of a porous morphology. Typically, this progression is followed by crystal development in the solvent or phase transition.[45] Heterogeneous shrinkage refers to the development of pores in a solid-state material as a result of mass or volume loss after non-equilibrium heat treatment.[46]

For the preparation of porous micro and nano-structures, chemical etching is a prevalent technique that exploits the differences in stability and solubility between the internal and external regions of crystals.[44] However, the nature of the starting template for self-templating strategies is usually homogeneous, and thus it is crucial to construct differences in stability and solubility between the internal and external regions of the self-templates. Cheng *et al.*[47] used NiMn-based glyceride as a template, given that it is generally believed that metal glycerides are unstable in water, and therefore will be etched by water solvent. As a result, the nickel manganese glycerate template was gradually eroded in *N*-methyl pyrrolidone and water solvent to form nickel manganese hydroxide. Therefore, after treatment in a mixed solution of *N*-methyl pyrrolidone and water, the NiMn-based glyceride templates were etched to form hierarchical hollow spheres. Due to the advantages of the unique porous structure and electrolyte contact area, the specific capacity of the nickel–manganese hydroxide hollow spheres as an electrode material was as high as 1680 F g^{-1} at 2 A g^{-1}. Niu *et al.*[48] prepared nickel hydroxide nanoplatelet arrays on the surface of nickel–aluminum foil by direct dealloying the foil in KOH solvent. In the presence of KOH, the aluminum foil components were easily etched, resulting in the formation of a layered porous structure on nickel–aluminum foils. Similarly, Zheng *et al.*[49] designed Ni$_{35}$Cu$_{15}$Zr$_{15}$Ti$_{35}$ metal glass ribbons as unalloyed precursors. Because of the different oxidation behaviors of Cu and Ni metals during dealloying and anodizing processes, NiO/Cu$_2$O heterojunctions with a hierarchical porous structure were successfully synthesized and applied in photo-assisted supercapacitors, providing an area capacity of 1182.2 F cm^{-3}. These demonstrations confirmed the viability of the etching approach as a strategy for synthesizing porous TM-based electrodes with superior electrochemical characteristics. Additionally, MOFs can be utilized as ideal alternatives for self-templating strategies. The ligand bindings between the majority of MOF metal ions and organic ligands are inadequately stable; thus, under acidic or alkaline conditions,

rapid hydrolysis causes the ligand bonds to eventually disintegrate the coordination structure.[50] Therefore, various porous structures have been prepared by etching techniques utilizing the inhomogeneity of MOF crystals. The inhomogeneity of MOF crystal structures usually originates from the uneven distribution of the metal–ligand bond density and defects along different crystallographic directions.[51,52] The anisotropy of the crystal structure results in exposed vertices, edges, and crystal surfaces having distinct chemical compositions; also, crystal surfaces exhibiting elevated densities of coordination bonds undergo preferred etching.[51] As shown in Fig. 1(a), in ZIF crystals, 2-methylimidazole coordination bonds are present on their {100} and {211} faces, whereas the {110} and {111} faces do not have these coordination bonds, and thus the etching process is preferentially started from the vertices on the {211} face.[10] Fig. 1(b)–(h) show the process of selective etching of a ZIF crystal. Etching the rhombic dodecahedron ZIF-8 or ZIF-67 at pH = 2.5 produced hollow ZIF-8 or ZIF-67 crystals with openings and thin walls, and the resulting crystals had the same side lengths as the corresponding initial crystals. These etch tests showed that etching occurs preferentially in crystallographic directions with more metal–ligand bonds; along these directions, the etch rate tends to be faster on higher dimensional crystalline surfaces; and etching can be adjusted by adjusting the pH of the etchant.

The outward diffusion method transfers mass from the centre region to the peripheral region more efficiently than selective etching to produce porous structures.[53] Recently, this technique has been widely reported for the preparation of porous TM-based electrodes, including Oswald ripening and sub-stabilized-directed secondary growth.[54] This approach, which does not require an external template, dramatically simplifies the synthesis strategy. Oswald ripening refers to the partial dissolution of less stable internal structures in a solvent and their redeposition on the crystal surface, resulting in the formation of a variety of porous structures on the micrometre and nanometre scales.[55] In the case of sub-stabilized-directed approved to secondary growth, it is the growth of crystals in the initially formed sub-stabilized state under thermodynamic conditions, which will further interact with the remaining reactants in the solvent, resulting in crystal growth. Zheng *et al.*[54] prepared an MnOOH precursor through Ostwald ripening, and then induced the escape of lattice oxygen by heat treatment, ultimately resulting in the formation of oxygen-defect-rich β-MnO$_2$ nanorods. Meanwhile, DFT calculations showed that the oxygen defects can act as dopants, leading to better electrical conductivity in β-MnO$_2$. The specific capacity of the assembled Zn//β-MnO$_2$ at 100 mA g^{-1} current was 330.9 mA h g^{-1}. Controllable interfacial ions can complete more complex structures. Tao *et al.*[21] successfully synthesized graphite-loaded Co and Ni multi-metallic hollow porous materials by utilizing an ion-exchange approach with thermal field modulation for the concentration dependence of the ZIF-67 zeolitic imidazolium skeleton, which is a porous cage-like structure and screened composites possessing extremely high electrical conductivity and abundant active sites. As shown in Fig. 1(i), polyhedral ZIF-67 was etched by Ni^{2+}. Specifically, the
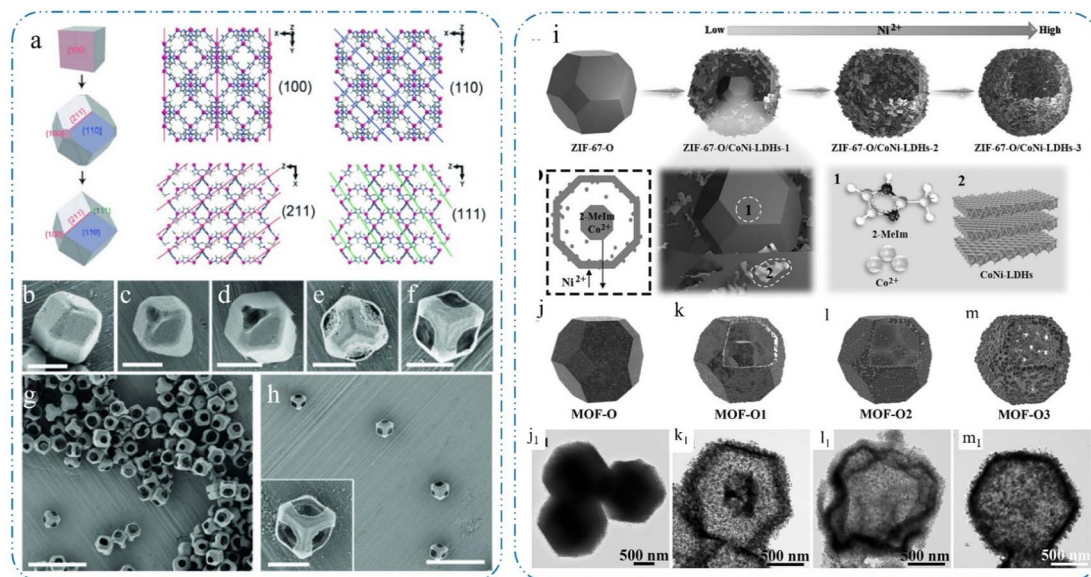
Fig. 1 (a) Schematic diagram of crystal morphology changes during the growth of ZIF-8 crystals. (b)–(f) Process of selective etching of ZIF crystals. (g) and (h) ZIF-8 crystals after etching completion, reproduced from ref. 10 with permission from [Wiley], Copyright [2015]. (i) Evolution path of the cavity. TEM images of (j) MOF-O, (k) MOF-O1, (l) MOF-O2, and (m) MOF-O3, reproduced from ref. 21 with permission from [Wiley], Copyright [2015].

protons in nickel ions etch the Co–N bonds from the outside in. Moreover, the escaping Co^{2+} assembles with the external Ni^{3+} (Ni^{2+} is oxidized) to form lamellar CoNi-LDHs. With a gradual increase in the nickel ion concentration, the solubility of the core increases, allowing the structure to evolve along a solid-like to core–shell to hollow pathway, as shown in Fig. 1(j–m), where MOF-O and MOF-O1 are solid and core–shell structures, while the rest are hollow. The type, content and distribution of chemical bonds in the precursor are influenced by the degree of ionic hybridisation, which can lead to sites and defects with inconsistent polarity upon pyrolysis.
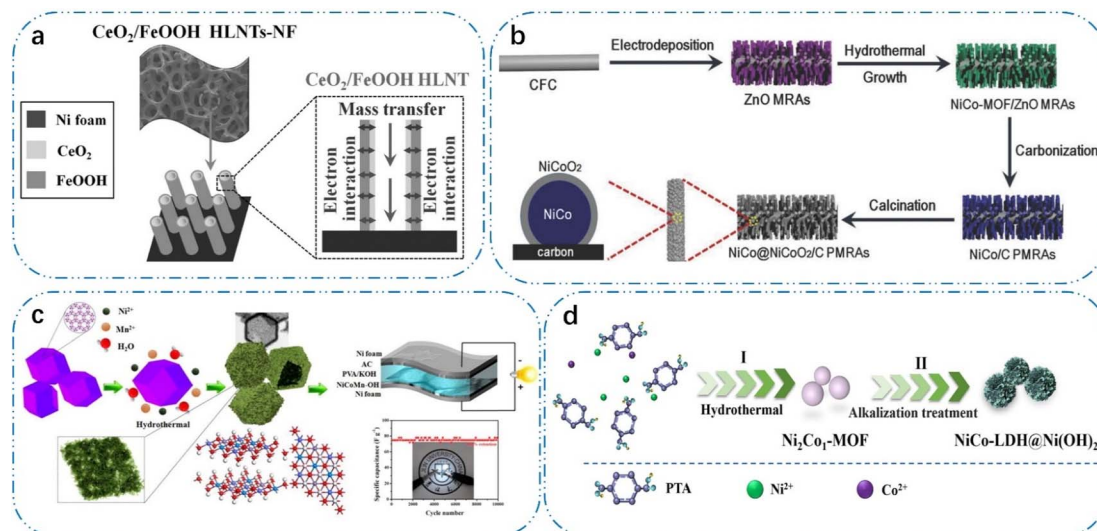
Thermal treatment conducted in an aerated environment can lead the progressive disintegration of solid macroparticles from their exterior to their interior, thus creating pores, and subsequently forming a canonical porous structure.[56] The synthesis of porous nanospheres with adjustable structures always involves the use of the heterogeneous contraction technique.[57] Different precursors have been utilized, including metal carbonates, glycerol, and metal–organic frameworks. Bie et al.[58] successfully synthesized $Zn_3V_3O_8$/C microspheres assembled from porous nanoplates via a thermal conversion strategy. Due to their porous structure, the nanorods exhibited an excellent capacity of 756 mA h g^{-1} at 0.4 A g^{-1}. Besides, heat treatment in noble gas can synergize dynamic oxidation with heterogeneous contraction, which can make the synthesized porous structure more controllable. Wang et al.[59] synthesized a CoO/C core–shell structure by carbonizing ZIF-67, in which both the core and shell were composed of cobalt oxide nanoparticles uniformly embedded in porous nitrogen-doped carbon. This unique structure maintained 96% capacity after 1000 cycles at 1 A g^{-1}.

2.1.2 Sacrificial template strategies. Currently, sacrificial template strategies, including hard and soft template routes, are considered to be the most straightforward methods for the synthesis of porous structures.[60] The most notable advantage of the sacrificial template strategy is that the dimension and morphology of the porous product can be easily controlled using different templates and adjusting the coating procedure.[61] Besides, the composition and porous structure of the product can be customized by selecting the appropriate template. The preparation of porous nanostructures with a controlled morphology and chemical composition is crucial for the electrochemical performance due to their influence on ion/electron transport and faradaic reaction processes.[62]

In the case of polymer analogues, the pyrolysis and escape of gases during carbonization by thermal conversion can result in the formation of abundant pores in carbon-based materials.[63] Moreover, soft and hard templates guide crystals to form structurally controlled pore structures.[64] Inorganic salts such as sodium chloride and potassium chloride may also be employed as templates in the synthesis of porous TM-based electrodes. This is due to the fact that water washing effectively eliminates the NaCl and KCl templates, hence significantly streamlining the preparation procedure.[65] For example, Hu et al.[66] prepared nitrogen and sulfur double-doped graphitic carbon nanoparticles with high porosity via the in situ growth of nickel-containing KCl-coated precursors. The layered structure with pores on the graphitic carbon nanosheets ensured sufficient contact with the electrolyte, thus providing enough active sites at the surface interface for electrochemical reactions. Given that ZnO materials are easily removed in alkaline solution or pyrolysis at high temperatures, ZnO is mostly used as a template for the preparation of TM-based electrodes.[67] As shown in Fig. 2(a) and (b), Li et al.[68] prepared a series of sandwich-like coaxial structures using ZnO, such as Cu-modified Ni_3S_2, FeOOH/Co/FeOOH nanotubes, FeOOH/CeO_2 heterostructured nanotubes,

View Article Online

Review | RSC Advances

Open Access Article. Published on 09 april 2024. Downloaded on 03.02.2026 16.56.55.
This article is licensed under a Creative Commons Attribution-NonCommercial 3.0 Unported Licence.

Fig. 2   (a) Microstructure and advantage of FeOOH/CeO$_2$ HLNTs–NF, reproduced from ref. 2 with permission from [Wiley], Copyright [2016]. (b) Schematic illustration of the fabrication of NiCo@NiCoO$_2$/C PMRAs, reproduced from ref. 14 with permission from [Wiley], Copyright [2018]. (c) Schematic diagram of the preparation process of Ni$_2$Co$_1$-MOF-derived nanosheet NiCo–LDH@Ni(OH)$_2$ heterogeneous composites, reproduced from ref. 26 with permission from [Elsevier], Copyright [2023]. (d) Schematic diagram of preparation process of NiCo–LDHs, reproduced from ref. 34 with permission from [Elsevier], Copyright [2019].

and carbon-coated NiCo@NiCoO$_2$ nuclear crust structure. Teng et al.[69] prepared Ni, NiSe$_2$, and NiFeO$_x$ and Ni$_2$P nanotube arrays using a ZnO template and phosphorylation strategy. The structure of the 3D nanotube arrays with porous structures and defects facilitated contact with the electrolyte, thus promoting electrochemical reactions and ion/electron transport.

Diatomaceous earth is a natural, low-cost inorganic material that can be supplied by diatomaceous earth mines or diatom farming. It is a siliceous sedimentary rock of biological origin. Diatomaceous earth is characterised by large internal space, high surface area and excellent biocompatibility due to its unique three-dimensional silica structure and nanoscale porous channels.[70] The natural porous structure of diatomite makes it a favourable choice for hard templates. It can provide broad active sites for the uniform distribution of nanomaterials along its surface and porous structure, which is conducive to the formation of conductive networks and solves the problem of agglomeration of nanomaterials.[71] Yi et al.[71] reported a versatile and scalable biotemplate-assisted strategy that employs naturally enriched diatomaceous earth as a growth template for the production of various TM nitrides. The conformal growth of nitride materials will cause them to inherit the morphological characteristics of the diatomite templates, resulting in the formation of structures with rich pore structures and abundant edge defects. Metal nitride devices with good electrical conductivity and solution-processable properties further facilitate the assembly of flexible, symmetric quasi-solid-state supercapacitor devices due to their excellent pseudocapacitive properties, which are stable under mechanical deformation. Given that simple one- or two-dimensional nanostructures have the drawback of agglomeration during their synthesis, the construction of three-dimensional porous nanostructures by the sacrificial template method can effectively solve this

problem. Li et al.[72] chose diatomaceous earth as a template and synthesised cobalt phosphide with diatomaceous earth morphology via a mild etching method using KOH hydro-alcoholic solution as an etchant. The introduction of P vacancies led to a decrease in the average oxidation state of the Co ions in V-CoP$_x$-1, which improved the electrical conductivity and provided more active sites for electrochemical reactions. Meanwhile, the introduction of P vacancies and V heteroatoms created more point defects and unpaired electrons, which improved the ionic conductivity of the material. The diatomaceous earth morphology of V-CoP$_x$-1 and the morphology transformation after reduction by NaBH$_4$ resulted in a larger specific surface area and higher porosity of the material. The synthesised V-CoP$_x$-1 exhibited an excellent performance of 829 F g^{-1} at 1 A g^{-1} and an improved cycling life of 80.84% of the original value after 10 000 cycles. Based on this, Li et al.[73] also synthesised phosphorus vacancy-modified CoP@FeP$_2$ heterostructures (pV-CP/FP) with a layered diatomite morphology through a series of chemical regulation methods. After replacing the oxygen atoms with phosphorus atoms by the calcination process, the phosphorus atoms in the formed TM phosphides heterostructures bonded the cobalt and iron atoms by interfacial bonding to form a heterojunction interface, which enhanced the charge transfer kinetics during the pseudocapacitive reaction. The layered structure of diatomite facilitated the electrochemical reaction of more –OH electrolyte ions on the surface of the phosphorus vacancy-modified CoP@FeP$_2$ heterostructure. As a result, the pVCP/FP$_2$ electrode exhibited a specific capacitance of 1028.8 F g^{-1} and 5 mV s^{-1}, excellent rate capability and good cycling performance.

Furthermore, MOFs can be used as precursors to create porous nanostructures as a self-sacrificial templates, and numerous techniques for synthesizing MOF porous derivatives

© 2024 The Author(s). Published by the Royal Society of Chemistry | RSC Adv., 2024, 14, 11482–11512 | 11487

have been devised.[62] As shown in Fig. 2(c), ZIF-67 was not only a template reactant but also provided a cobalt source. Subsequently, additional nickel nitrate and manganese chlorate were added, and in a hydrothermal reaction, the protons generated by the hydrolysis of nickel and manganese ions are thought to etch ZIF-67 by substituting the 2-methylimidazole anion. Meanwhile, the Co^{2+} generated by ZIF-67 is partially oxidised by NO^{3-} and O_2 to form Co^{3+}, after which Co^{2+}/Co^{3+}, Ni^{2+} and Mn^{2+} co-precipitate to form hollow nickel–cobalt–manganese hydroxide polyhedra, and ultrathin stacked nanosheets constructed at the 3D porous ordered polyhedral structure with porous channels inside them to facilitate electron/ion transfer.[74] Subsequently, similar synthetic strategies were used to produce other LDHs and metal hydroxides. As shown in Fig. 2(d), the classical multimetallic MOFs were synthesised via the solvothermal method with nickel and cobalt as bimetallic cations to obtain MOF precursors with different Ni/Co ratios. Subsequently, an alkaline oxidation environment was constructed, in which the prepared NiCo-MOF powder samples were placed, and the NiCo-MOF materials were transformed into nanosheet NiCo-LDH heterocomposites. Meanwhile, the process of MOF-derived LDH can be observed by in situ characterization techniques, and Wang et al.[75] observed the conversion of ZIF-8 nanocubes and rhombic dodecahedra to LDH by in situ TEM. The metal ions of MOFs can be converted to TM oxides by oxidation and thermal conversion in air, and thus MOFs are also well suited as sacrificial TM oxides for the production of various porous TM oxides as sacrificial templates. Li et al.[76] prepared a novel petal-like N-doped porous carbon embedded with ultrafine cobalt oxide nanoparticles via the pyrolysis of an N-rich Co-MOF, whose unique layered structure, abundant active sites and large specific area contribute to the improvement in energy storage performance. Li et al.[77] prepared Fe_2O_3/Fe_3O_4 octahedra with a porous morphology. In addition, different porous TM oxides such as ZnO,[78] CeO_2,[79] and In_2O_3 (ref. 80) were synthesized using different MOF precursors.

2.2 Thermal conversion strategy

Given that the formation of crystallinity, crystal grain size and morphology can be effectively controlled, the thermal conversion strategy is also widely used for the preparation of TM-based electrodes. During the thermal conversion process, the precursors are treated at high temperatures, and a large number of pores is created in the final crystals due to the escape of gases during pyrolysis or the removal of surfactants. Additionally, the high-temperature thermal conversion enhances the degree of crystallization of porous TM-based electrodes, thereby improving the cycling stability of the products that are produced.[81] Gas pyrolysis and solvent thermal conversion are the thermal conversion methods that have received the most research interest. When preparing porous TM-based electrodes via gas pyrolysis, thermal conversion is often accomplished with the TM vapors present in the gas. Alternatively, solvent thermal conversion involves the introduction of TM ions in the solvent. Thermal conversion is one of the important research topics in the fabrication of porous TM-based electrodes. The controllable

and stable structure, as well as their straightforward synthetic process, are all advantages of these electrodes.

Carbon materials significantly impact the energy storage performance of porous TM-based materials. Although these materials exhibit considerable potential as electrodes for double layer capacitors, they are limited in energy density.[82] Numerous approaches are utilized to enhance the characteristics of TM composites through carbon doping.[83] One of these approaches is thermal conversion, which combines carbonization and thermal conversion under the influence of temperature. To enhance ion/electron transport pathways and augment surface interface active sites, many studies have focused on the fabrication of porous carbon–TM blends with high electrochemical activity and excellent electrical conductivity. Sun et al.[84] synthesized composites of TM oxides and nitrogen-doped carbon by chelating TM ions by EDTA-2Na followed by carbonization. The prepared CoO_4–N–C exhibited excellent electrochemical properties. DFT calculations showed that the porous structure of cobalt oxide and the complexation between N–C provided more active sites and are more favourable for redox reactions. The activation of biomass is crucial for the formation of pores and increase the surface area of electrode materials. Yan et al.[85] used hibiscus flowers as the raw material and potassium hydroxide as the activator. A two-step method of high-temperature precarbonisation-activation was used to prepare hibiscus flower-based porous biomass carbon with large specific surface area and excellent performance. The elemental composition and structural characteristics as well as other physical and chemical properties were characterised by electrochemical tests to explore the energy storage performance of hibiscus flower-based biomass carbon as an electrode material. Thus, it is expected that waste can be converted into valuable materials and provide biomass carbon for energy storage. The resulting biomass is considered to be a resource recycling, environmentally friendly and high-performance electrode material. Acid–base reactions involving organic bases (melamine, dicyandiamide, aniline, etc.) and organic acids (sulfonic acids, boric acids, carboxylic acids, etc.) result in the formation of self-assembled extended cross-linked polymers in aqueous solvents. These polymers are enriched in functional groups that are amenable to coordination with metal ions. Carbon materials doped with heteroatoms can be generated through subsequent thermal decomposition and carbonization under inert gas conditions.[86] For instance, Yuan et al.[87] prepared CoP crystals on porous carbon doped with nitrogen and phosphorus, which possessed faster ion transport pathways with higher electrochemical activity than CoP porous carbon mixtures in acidic media.

Besides unitary porous TM-based electrodes, several heteroatom-doped combinations of polymetallic materials demonstrate exceptional electrochemical characteristics.[88] For the synthesis of porous materials composed of hybrid metals, high-temperature thermal conversion is a more facile and operative method than alternative synthesis approaches. The advantage of the thermal conversion strategy over other preparation strategies is its simplicity and efficiency for the synthesis of TM-based porous materials. Yang et al.[89] prepared

porous Fe/Co–N–C *via* the carbonization of polypyrrole hydrogels with iron and cobalt. This supramolecular crosslinked polypyrrole hydrogel could efficiently sequester cobalt and iron compounds. Compared to conductive polymers, Prussian blue analogs (PBA) have an open backbone structure and are commonly used to prepare TM-based electrodes that are enriched with redox active sites and strong structural stability. Jia *et al.*[90] prepared carbon dot/phosphated nickel–iron nanoparticles grown on nickel foam by directly phosphating PBA. It was found that the doping of carbon quantum dots not only promoted the growth of nanocubes on the PBA precursor, but also alleviated the aggregation of the nanocubes during thermal decomposition. Furthermore, the fabricated hybrid supercapacitors showed remarkable multiplicative performance and excellent cycling stability. Meanwhile, Kumar *et al.*[91] prepared porous FeNi oxide nanocubes *via* the thermal treatment of NiFe–PBA in air. The prepared material possessed hybridized phases of nickel oxide and iron oxide with a specific surface area of 30 m^2 g^{-1}. Besides high porosity and a porous structure, which enhance ion transport, the active sites exposed at the crystal vertices and edges significantly increase the redox activity.

Moreover, when used as templates for the thermal conversion of polymetallic materials, MOFs are also suitable as templates for most thermal conversions due to their highly tunable chemical composition and structure.[92] By subjecting MOFs to heat treatment in various atmospheres, it is possible to produce numerous functional materials generated from MOFs, including carbon-based compounds, metal-doped carbon-based compounds, and TM-based compounds. Furthermore, porous TM-based electrodes with various morphologies, such as particles, quantum dots,[93] nanowires, nanosheets, and mesh structures, can be produced by engineering the precursor morphology of MOFs, given that the morphology of MOFs can be effectively maintained throughout the thermal conversion process. As shown in Fig. 3(a), Gu *et al.*[6] synthesized a nanocomposite of Ni–CoP and CNTs by annealing ZIF-67 for 2 h under a nitrogen environment, embedding the Ni-doped CoP in an amorphous carbon matrix, and then anchoring it on the surface of CNT. The composite of Ni–CoP@C with CNT backbone endowed it with a richer internal porosity. This allowed for more efficient ion/electron transfer and buffered internal stresses to fully utilize the pseudocapacitive properties of the phosphide. According to DFT calculations, the realization of Ni doping by the ion-exchange process of ZIF-67 in the solvent contributes to the ion/electron transport behaviour of Ni–CoP in electrochemical reactions. Metal cations in MOFs can also induce the growth of CNTs. As shown in Fig. 3(b), Cao *et al.*[13] reported the construction of 3D carbon nanotube networks *via* an MOF-induced method. ZIF-67 was used as a precursor and melamine catalyst was added to control the directional growth of carbon nanotubes by thermal conversion. The 3D carbon nanotube network was assembled from 1D carbon nanotubes with an adequate pore distribution. Considering the importance of the optimal structure for the electrochemical performance, some studies prepared self-supporting electrodes composed of MOFs. For example, Li *et al.*[94] prepared a large

number of hollow polyhedra containing N-doped carbon nanotubes and Co_3O_4 nanoparticles (Co_3O_4 NPs) on bio-templates *via* a thermal conversion strategy. The *ortho*-polyhedra were uniformly arranged on the outer surface of diatomaceous earth with a natural porous structure, aiming to avoid the agglomeration of carbon nanotubes. The results of electrochemical tests showed that the composites have good electrochemical properties, as evidenced by their high specific capacity of 894.6 F g^{-1} at 2 A g^{-1}, good multiplicity performance and high cycling performance. Ma *et al.*[95] prepared Co_3O_4/carbon porous nanorod arrays by pyrolyzing MOFs directly grown on copper foil under a nitrogen atmosphere. Also, porous nanowires with more active sites and higher porosity were produced during the thermal conversion process. Pre-treatment of MOFs by ligand exchange reaction allows the doping of other TM during thermal conversion. As shown in Fig. 3(c), Hu *et al.*[27] prepared iron-doped CoP nanosheet arrays on nickel foam by subjecting ZIF-67 to a ligand–exchange reaction in aqueous $K_4[Fe(CN)_6]$, followed by phosphorylation in N_2. The combination of its porous nanoshells and pore interior provided sufficient active sites and efficient electron transport pathways.

Solvent thermal conversion has been exploited to simulate the crystal growth conditions, where the initial high temperatures and pressures substantially accelerate the reaction rate and afford regulation of the end product. Water is commonly employed as the solvent of choice, enabling the formation of a variety of porous structures. Solvothermal conversion permits modifications to the phase and composition of the generated materials, where the regulation of the micro and nanostructures of the crystals results in enhanced electrochemical performances. Ma *et al.*[96] used a hydrothermal technique to vary the ratio of cobalt acetate to carbon disulfide to prepare a variety of cobalt sulfide compounds. The abundant porosity and unique crystal structure together determine the electrochemical properties of the prepared compounds. The preparation of electrode materials with high electrochemical performance can be achieved effectively by creating defects and vacancies in the electrode material.[97] Wang *et al.*[98] prepared phosphorus-doped Co_3O_4 nanowires on nickel foam with a porous structure, where their 1D structure with high porosity greatly facilitated electron transport and active site exposure. However, the agglomeration effect of one- or two-dimensional structural materials during thermal conversion affected the electron transport during charge/discharge cycling. Thus, Li *et al.*[99] synthesised FeOOH nanorods and PPy nanoparticles modified on diatomaceous earth *via* a two-step hydrothermal and *in situ* polymerisation route to form a ternary complex of core/shell/shell D@FeOOH@PPy. Diatomaceous earth served as the backbone, and FeOOH and PPy provided a large number of mesopores after being bonded together *via* Fe–N chemical bonds. In addition, the polymerisation process of the PPy layer introduced some oxygen vacancies based on low-valent Fe^{2+}. Finally, the D@FeOOH@PPy electrode exhibited a better electrochemical performance in terms of specific capacitance, conductivity, structural stability and cycle life compared to D@FeOOH. To better increase the energy density of supercapacitors, the synergistic effect of multiple TM is crucial. Based
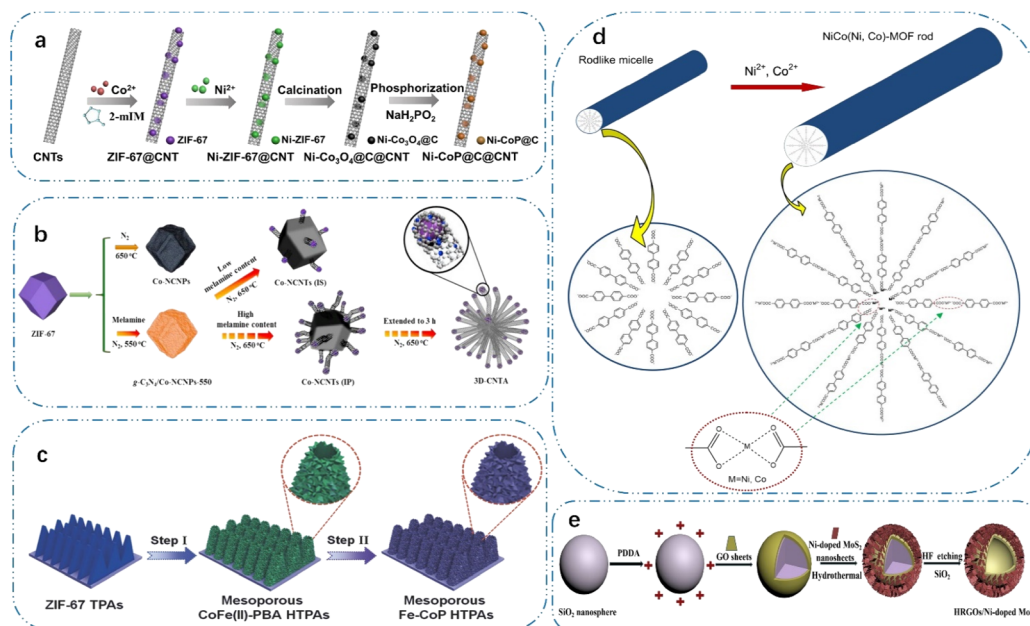
Fig. 3 (a) Schematic illustration of the fabrication process of Ni-CoP@C@CNT, reproduced from ref. 6 with permission from [Elsevier], Copyright [2020]. (b) Schematic illustration of the formation process of 3D-CNTA, reproduced from ref. 13 with permission from [Elsevier], Copyright [2017]. (c) Schematic illustration of the construction of mesoporous Fe−CoP HTPAs, reproduced from ref. 27 with permission from [Wiley], Copyright [2018]. (d) Schematic of the growth process of NiCo(Ni,Co)-MOF rods, reproduced from ref. 36 with permission from [Elsevier], Copyright [2019]. (e) Schematic diagram of synthetic process for HRGO/Ni-doped MoS$_2$ composite, reproduced from ref. 39 with permission from [Elsevier], Copyright [2020].

on this, Li *et al.*[100] also successfully realised the transformation process from MnO$_2$ to FeOOH on diatomaceous earth *via* a two-step hydrothermal method and obtained derivatives with three-dimensional diatom morphology by an etching process. The prepared MnFeO$_x$-0 diatomite derivatives consisted of MnO$_2$ nanosheets with a high specific capacitance (228.6 F g^{-1} at 1 A g^{-1}), good rate capability (capacitance retention of 74.6% after the increase of the current density to 10 A g^{-1}), high coulombic efficiency (about 93.1% at 10 A g^{-1}), and stable cycling performance (capacitance retention of 94.3% after 4000 cycles).

Also, the solvent thermal conversion method has been extensively employed for introducing metal ions from the solvent into porous TM-based electrodes. As shown in Fig. 3(d), Wang *et al.*[36] synthesized 3D porous NiCo bimetallic materials with high crystallinity and stability *via* hydrothermal synthesis. According to the results of electrochemical tests, the reduced intrinsic resistance, charge transfer resistance, and ion diffusion impedance of the polymetallic material contributed to its higher capacity at various current densities. Furthermore, the construction of heterogeneous structures is also a promising strategy for the fabrication of polymetallic TM-based electrodes. In a study by Fu *et al.*,[101] Ni$_3$N-NiMoN heterostructures were prepared *via* a hydrothermal nitriding strategy of the precursor, and its heterogeneous structure could not only realize the promotion effect among the components, but also the exposed active sites in the 2D porous structures are one of the reasons for their high electrochemical reactivity. Furthermore, the construction of 2D structures *via* thermal conversion could also

effectively enhance the ion transport and expose the active sites. Although layered double hydroxides have good electrochemical properties, their cycling stability is poor and they are prone to self-stacking. In this case, it is an efficient technique to build core–shell structures using various components to enhance their electrochemical qualities. Through a hydrothermal-phosphatization strategy, Zhang *et al.*[102] prepared an NiFe-LDH@NiCoP core–shell structure. The self-supporting structure with porous properties significantly increased the exposed active sites and ion/electron transport pathways. The electronic interactions in the NiFe-LDH@NiCoP composite promoted the charge transfer and enhanced the reaction kinetics. Additionally, the stacking of porous 2D nanosheets to create a structure akin to a nanoflower facilitates the penetration of the electrolyte, exposing more active sites and improving the electrochemical performance. Dinh *et al.*[103] synthesized NiFeV-LDH on nickel foam and the connections between these nanosheets formed a hierarchical porous structure. Besides, doping could also improve its electrochemical reactivity. For example, cobalt can also be used as a dopant to prepare NiFeCo-LDH.[104] The activity of the 2D lamellar structure of MoS$_2$ originates from the sulfur atoms at its edge sites, but how to excite the inert sulfur atoms becomes a problem. As shown in Fig. 3(e), Chang *et al.*[39] created rGO/Ni-doped MoS$_2$ with a hierarchical nanoflower structure using hydrothermal techniques and self-assembly strategies. The rGO/Ni-doped MoS$_2$ composites exhibited improved multiplicative properties, outstanding cycling stability, and a higher specific capacitance of 544 F g^{-1} at

1 A g^{-1}. This is because porous nanoflower structures and polymetallics work synergistically to create a powerful effect.

2.3 Chemical deposition strategy

The chemical deposition strategies for building ideal structures and interfaces by reacting on different substrate surfaces mainly include chemical vapor deposition and electrochemical deposition. The structure and size of the products are highly tunable by controlling different reaction parameters. Compared with other TM-based material preparation strategies, chemical deposition strategies can build ordered porous structures more precisely, efficiently, and scalably. This chapter summarizes some TM-based electrode materials prepared by chemical deposition strategies.

2.3.1 Chemical vapor deposition. During chemical vapor deposition, gaseous substances react on the surface of a substrate to produce solid deposition products. The regulation of the growth parameters, including the source material quantity, source pressure, temperature and pressure, allows the manipulation of the product attributes including number of layers, size, morphology, and orientation.[105] Also, it makes the introduction of doping or defects possible. Prior to the widespread adoption of chemical vapor deposition, mechanical stripping and liquid phase stripping were the predominant techniques employed to fabricate 2D porous materials. However, these approaches are characterized by their low throughput and the challenge of precisely controlling the size and porous structure of the final samples. Consequently, chemical vapor deposition has emerged as a scalable and efficient alternative for fabricating large-area porous structures that possess a significant degree of flexibility.[106]

To ensure product homogeneity, the metal–organic compound chemical vapor deposition (MOCVD) strategy uses a high-purity metal–organic or compound gas as the precursor for gas-phase epitaxial growth *via* thermal treatment. It is widely used to prepare low-dimensional materials such as TM compounds because its components and interfaces are highly controllable.[107] By thermal treatment of metal–organic compounds, metal–organic compound chemical vapor deposition technology enables the gas-phase epitaxial development of metal–organic compounds, where a precursor consisting of a highly pure metal–organic compound gas guarantees product homogeneity. Its broad application in the fabrication of low-dimensional substances, including TM compounds, is attributed to the fact that its constituents and interfaces are exceedingly versatile.[108] As shown in Fig. 4(a), Kang *et al.*[4] used the metal–organic compound chemical vapor deposition strategy to prepare MoS_2 with a size of 10 cm on an SiO_2/Si substrate; however, the low reactant flux resulted in the slow growth rate of the product. Thus, it is necessary to reduce the energy consumption of the reaction process. As shown in Fig. 4(b), to precisely regulate the variables in the reaction, Kalanya *et al.*[22] designed a novel growth system called pulsed metal–organic compound chemical vapor deposition (PMECVD). In this system, solid organic precursors are sublimated into the reaction chamber, and then discretized, and the system corrects the
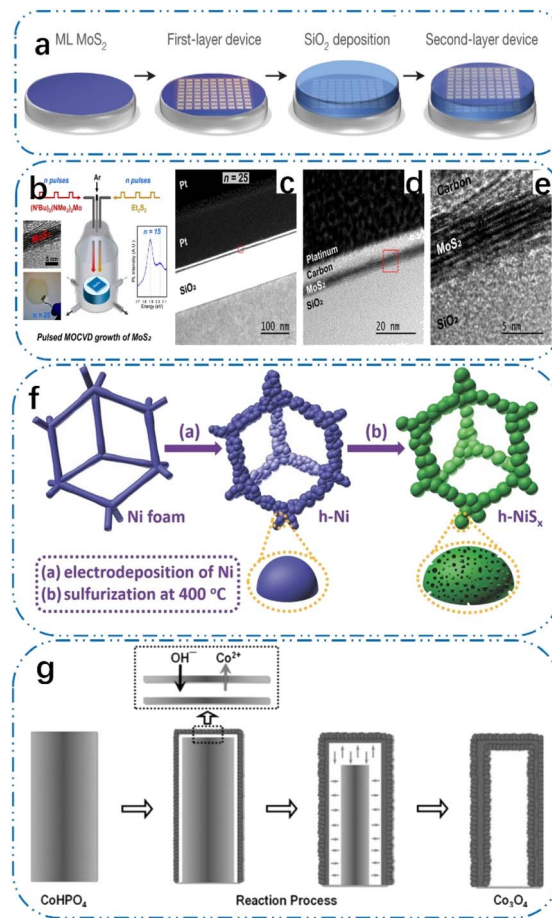

Fig. 4 (a) Schematic illustration of MoS_2/SiO_2, reproduced from ref. 4 with permission from [Nature], Copyright [2015]. (b) Schematic of reactor geometry and (c)–(e) HRTEM cross sections from MOCVD-grown MoS_2 on SiO_2/Si, reproduced from ref. 22 with permission from [the American Chemical Society], Copyright [2017]. (f) Schematic of the preparation of h-NiS$_x$: (a) template-free electrodeposition of metallic Ni microsphere arrays and (b) sulfurization, reproduced from ref. 25 with permission from [Wiley], Copyright [2016]. (g) Schematic illustration of the formation of Co_3O_4-MTA from the original $CoHPO_4$ microrods, reproduced from ref. 32 with permission from [Wiley], Copyright [2017].

pulses of each part of the precursor. The system corrects the pulse of each part of the precursor to realize the precise control of the variables in the reaction, and the system can synthesize an MoS_2 film with a size of 5 cm in 90 s, which greatly reduces the growth time and the power consumption. However, its reproducibility is poor because it is difficult to regulate the rate of the pyrolysis of the precursor during the heat treatment procedure. Choi *et al.*[109] used liquid organic compounds instead of solid ones, which ensured the homogeneous delivery of the reactants, and the area covered by MoS_2 in the reaction increased linearly with the growth time, and an MoS_2 film with the size of 2 cm was synthesized in about 15 min. Although the reaction rate and product area were not as high that in the first two methods, the liquid-phase precursor made the reaction process simpler and improved the experiment reproducibility. Given that carbon will be generated during the reaction process

and doped into the products due to the elemental complexity of the precursor containing organics, the metal–organic compound chemical vapor deposition strategy has great potential for the preparation of 2D porous materials. However, the yield quality will be poor due to this carbon doping.

Although MOCVD can be employed to rapidly prepare large-area 2D materials, its deposition rate is slow and it is only suitable for depositing micron-sized surface layers, and the low pressure and flammable gases keep the growth device in an unstable state.[110] Conventional chemical vapor deposition (CVD) strategies share similar growth principles with metal–organic compound CVD, but their precursors are usually inorganic, and thus the products are not carbon doped, and the reaction process does not require harsh low-pressure conditions, simplifying the preparation strategy. Meanwhile, conventional CVD techniques control the size, quantity of layers, and quality of the products by adjusting the CVD parameters, and the products usually have lower grain boundary densities than that produced by metal–organic CVD. Lv et al.[111] used CVD to deposit graphene coatings on nickel foam, which were then thermally converted by solvent to bare nickel. Then, a large number of nanowire aggregates formed flower-like $ZnCo_2O_4$ microspheres on bare nickel foam via solvothermal conversion, and large-scale arrays of $ZnCo_2O_4$ nanowires were uniformly aligned and sufficiently segregated on the graphene-coated nickel foam. The $ZnCo_2O_4$ nanowire structures exhibited an excellent energy storage performance, which promoted electrolyte infiltration and electron transport. Furthermore, the substrate used for current collection has better conductivity when graphene is present. The selection of substrates with a wider pore size distribution can effectively improve the aggregation of electrode materials and lower intrinsic conductivity. Li et al.[112] overcame these challenges by synthesising nickel–iron sulphide nanosheets ($NiFeS_x$) and carbon nanotubes (CNTs) on diatomaceous earth using chemical vapour deposition and a two-step hydrothermal method. The synthesis of this composite successfully exploited the synergistic effect of multi-component materials to improve the electrochemical properties. The choice of diatomaceous earth as the substrate provides a favourable environment for the uniform dispersion of nanomaterials on its surface, which expands the active sites in contact with the electrolyte and significantly improves the electrochemical performance. Combining the high conductivity and the simultaneous vulcanisation effect, the $NiFeS_x$@CNTs@MnS@diatomite electrode provided a high specific capacitance of $552F\ g^{-1}$ at a current density of $1\ A\ g^{-1}$ and a good multiplicative performance of 68.4% at $10\ A\ g^{-1}$. Warwick et al.[113] prepared nanostructured films of vanadium oxides using electric field-assisted CVD. Scanning electron microscopy, X-ray diffraction, Raman spectroscopy, and X-ray photoelectron spectroscopy were used to characterize the membrane. These techniques showed that the membrane had an open, porous morphology with a few surface features (5 nm). The prepared films were later assembled into supercapacitors, and specific capacitances of up to 3700 μF cm^{-2} were obtained by cyclic voltammetry.

2.3.2 Electrochemical deposition. Electrochemical deposition is a highly efficient technique utilized in the fabrication of self-supporting electrodes through the deposition of metalized films on various substrates. During this procedure, the active material is directly applied to the electrode surface through the use of cathodic or anodic electrolysis in the appropriate complex or salt solution. Furthermore, the formation of porous structures within the metal film is facilitated by the in situ generation of bubbles under the polarized conditions that occur during electrodeposition.[114] Furthermore, by manipulating the electrochemical deposition conditions (e.g., current density, solvent, deposition potential, and time), the morphology and thickness of the metal film can be precisely adjusted. Because it removes the need for a binder in the prepared electrodes, this adjustment improves the active surface area, conductivity, and electrochemical performances of the electrodes.[115]

Reactive surfaces that form over time in electrode materials are essential for increasing the energy density of supercapacitors. As illustrated in Fig. 4(c), Sun et al.[25] prepared porous 3D nickel spheres on nickel foam via electrochemical deposition, and subsequently phosphorylated them under low-temperature conditions to obtain sea-urchin-like Ni_2P on nickel foam. Its three-dimensional porous structure allowed for both effective mass transfer and the exposure of the active sites, which resulted in very high electrochemical activity and long cycle stability. Similarly, porous nickel sulfide structures on nickel foam could be obtained by electrochemical deposition followed by sulfidation in a similar strategy.[25] Cobalt-based materials are widely prepared using electrochemical deposition strategies. Zhu et al.[116] prepared CoP porous nanorod arrays on nickel foam via constant-potential electrochemical deposition in a three-electrode system. The aggregation of nanoparticles formed a surface with a large number of mesopores, which revealed the preparative advantages of electrochemical deposition in terms of controllability of the electrode structure. However, the porous structure prepared by electrochemical deposition from nanosheet stacking is stoichiometric and inhomogeneous. As shown in Fig. 4(d), Zhu et al.[32] prepared hollow Co_3O_4-derived Co_3O_4-MTAs using a simple electrochemical self-templating strategy. These Co_3O_4-MTAs had a surface area of $233\ m^2\ g^{-1}$ and a hollow porous structure, which improved the mass transfer rate and allowed for long cycle stability and excellent electrochemical activity.

In contrast to porous materials composed only of TM, the introduction of additional TM elements in these materials may induce synergistic effects that enhance their electrochemical performance. For example, in the fluorinated nickel–iron oxide porous film prepared by electrochemical deposition and anodic treatment,[117] the fine nanoporous structure of the porous film offered a large number of active sites for the electrochemical reaction, and the synergistic fusion of its composition and structure enhanced the overall electrochemical performance of the electrode, in addition to enhancing the highly efficient electrochemical reaction. Xiao et al.[118] prepared $(Ni,Co)_{0.85}Se$ nanoplatelets on nickel foam via electrochemical deposition and solvent thermal conversion strategies, which provided

activity for the overall electrochemical reaction. Furthermore, Ye et al.[119] prepared metallic nickel–cobalt thin films on titanium foam using constant current density electrodeposition, and the micro–nanostructures of the porous films could be well controlled by controlling the electrochemical deposition time. In addition to TM phosphides, the overall electrochemical properties of TM phosphates have great potential. Through electrochemical deposition in metal chlorides and sodium hypophosphite solvents, Lei et al.[120] prepared porous nickel–iron hydroxyphosphates on nickel foam. The porous stacked nanosheets possessed interconnected channels, which greatly increased the specific surface area and facilitated ion/electron transport. In supercapacitor electrode materials, layered double hydroxides (LDHs) also show significant promise. NiFe-LDH nanoplatelets grown on Cu foam were prepared by Ren et al.,[121] where this self-supporting structure had a large specific surface area, open channels, and good electrochemical performance.

The electrochemical deposition strategy is a straightforward and high-throughput method for creating various porous TM-based electrodes with a chemical composition and structure that can be manipulated. However, there are still certain disadvantages with the electrochemical deposition strategy, which restrict its application. For instance, the metal films acquired on various substrates typically exhibit inadequate crystallization and are susceptible to dissolution when exposed to elevated voltages or current densities. Alternatively, electrochemical deposition is not as frequently used in the preparation of TM nitrides and carbides. Consequently, a two-step approach that integrates electrochemical deposition with additional synthesis strategies can yield a porous structure that is more amenable to control.

2.4 Guest–host hybridization strategy

Because of their diverse morphologies, composite forms, good coordination with other substituents, large specific surface area, adjustable structural defects, and high energy density, TM-based electrode materials have emerged as one of the most promising materials for supercapacitors.[122] Due to their abundance of unpaired d-orbital electrons, single TM such as iron, cobalt, nickel, copper, and molybdenum, as well as their alloys, oxides, sulfides, nitrides, and phosphides, have been studied in great detail and exhibit strong electrochemical activity. However, because of their structural complexity, physicochemical difficulties, and thermodynamic instability, TM exhibit poor electrical conductivity and cycling stability.[123] In this case, the guest–host hybridization strategy is one of the effective ways to improve the electrochemical properties of TM electrode materials by compositing TM or their compounds with highly conductive and stable materials, such as carbon-based nanomaterials. It can divided into two types, where one is connected by relatively weak chemical bonds, such as van der Waals force, hydrogen bonding, and weak electric field, and the other is connected by stronger chemical bonds, such as covalent bonding.[124]

The advantages of carbon as an electrode material are its high electrical conductivity, adjustable physicochemical properties, ability to be fast charging and discharging, long cycle life and stable structure.[125] Graphene, carbon nanotubes, and carbon derived from biomass are examples of carbon materials with varying dimensions, structures, and morphologies that have been effectively utilized in supercapacitor research for the creation of carbon-based electrodes. Generally, the majority of research showed that the porosity of TM electrode materials significantly affects their overall electrochemical performance.[126] The electrolyte ions can readily and rapidly submerge into an active electrode material whose size corresponds to the porosity of the structure because the wettability of the electrode material with the electrolyte depends on its porosity.[127] For example, Zhang et al.[128] discussed in detail the porosity of TM-based electrode materials and considered various key aspects of the nano–mesoporous structure, where it is the electrically active surface area with a large number of pores accessible to the electrolyte that positively affects the specific capacitance.[129] For example, Li et al.[130] synthesized carbon nanosphere composite nickel–cobalt oxide double-shell hollow spheres via solvothermal conversion using a novel chemical method. In the double-shell nickel–cobalt oxide hollow spheres, the capacity increased from 445 F g^{-1} to 718 F g^{-1}, while the specific surface area increased from 76.6 m^2 g^{-1} in single-shell nickel–cobalt oxide hollow spheres to 115.2 m^2 g^{-1}. Porous composites of TM and carbon can also increase the operating voltage of supercapacitors, as illustrated in Fig. 5(a). Zang et al.[9] coated titanium disulfide on vertically aligned carbon nanotubes, and this composite electrode not only had a good electrochemical performance, but also stabilized the operating voltage above 3 V. At the same time, this nanostructure promoted the ionic transport and surface interface activity, and it also caused excellent cycling stability (10 000 cycles at 12 000 W kg^{-1}). However, the cycling performance of the aforementioned nanocomposites did not improve much. Moreover, the additional synthesis of conductive phases and further coupling methods, although helpful in changing the conductivity of TM-based materials, still need to address the lattice volume expansion and contraction phenomena occurring during their recharge and discharge processes entirely. Zhang et al.[131] successfully synthesized ZIF-67-derived N-Co$_3$S$_4$-GN/CNT conductive networks via thermal conversion in a gas with the optimal synthetic parameter settings determined. The graphene and carbon nanotubes were grown in situ by cobalt ion catalysis in ZIF-67, and given that they were grown in situ and not added, the interfacial bonding was quite strong, and the capacitance loss was only 2.8% after 4000 cycles at 1 A g^{-1}, which suggested the cycling stability of TM sulfides. Yan et al.[132] successfully synthesised SiO$_2$@Co$_3$O$_4$/GA composites with a bilayer structure via an in situ self-assembly method. Microstructural measurements showed that the SiO$_2$ film encapsulated Co$_3$O$_4$, and then anchored together on the folded GA to achieve re-encapsulation. A more stable Si–O–Co could be formed using this preparation process, and thus its performance was significantly improved. This structure not only improved the
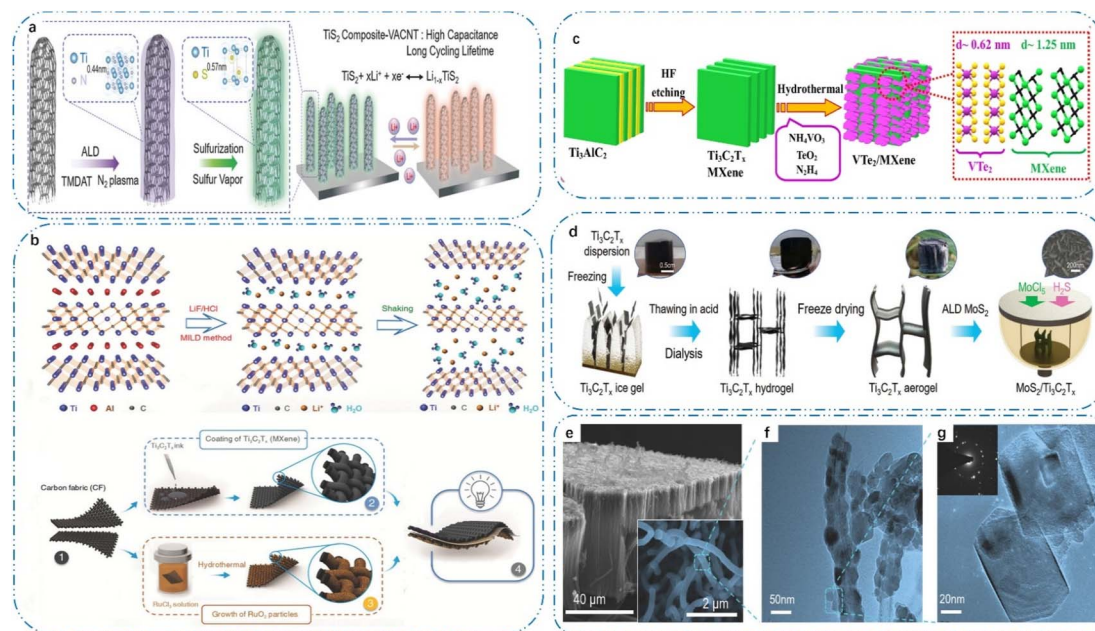
Fig. 5 (a) TiS$_2$-VACNT composite electrodes synthesized *via* a two-step process, reproduced from ref. 9 with permission from [Wiley], Copyright [2018], (b) synthesis scheme of Ti$_3$C$_2$T$_x$ MXenes and schematic illustration of the synthesis method of the VTe$_2$/MXene heterostructure, reproduced from ref. 16 with permission from [Wiley], Copyright [2018]. (c) Schematic representation illustrating the process for the fabrication of an asymmetric supercapacitor, reproduced from ref. 24 with permission from [The Royal Society of Chemistry], Copyright [2022]. (d) Schematic illustration of the process for the preparation of MoS$_2$/MXene hybrid aerogel, reproduced from ref. 31 with permission from [Wiley], Copyright [2022]. (e) SEM image after a 500-cycle ALD TiN deposition process, followed by a sulfurization step; inset: magnified SEM image showing individual electrodes with a diameter of 210 ± 13 nm, reproduced from ref. 31 with permission from [Wiley], Copyright [2022]. (f) TEM image of CNT coated with sulfurized TiS$_2$ composite particles. (g) Zoomed-in TEM image of hexagonal TiS$_2$ composite nanoparticles.

capacitance of GA, but also effectively reduced the bulk expansion and aggregation of Co$_3$O$_4$.

MXenes are highly promising materials as electrodes for the fabrication of supercapacitor devices due to their exceptional redox activity, compositional diversity, and high electrical conductivity.[133] However, high-performance supercapacitors require electrode materials that have good cycling stability, a large capacity for charging storage, and excellent electrical conductivity for quick electron transfer. However, although MXenes have many of these properties, they undergo irreversible oxidation below and back at the anodic potential, and their narrow electrochemical stabilization potential window limits their energy storage capacity.[134] In this case, although TM usually have high redox activity, they are limited by their cycling stability and poor reproducible performance in terms of lower electrical conductivity and solubility in aqueous electrolytes. These challenges limit their wide application. The formation of heterostructures of TM with MXenes and using asymmetric electrode structures is a feasible strategy to address these limitations. This strategy not only improves the cycling stability and reproducible performance of TM but also increases the charge storage capacity of MXenes.[135] Based on the fact that titanium carbide can function at a negative potential in an acidic electrolyte, as illustrated in Fig. 5(b), by mixing an MXene with RuO$_2$, Jiang *et al.*[16] created fully pseudocapacitive supercapacitors. The operating voltage window of the asymmetric electrodes was 1.5 V, which is roughly twice that of the

symmetric supercapacitors. The overall performance of the devices could be greatly enhanced by the proton-induced pseudocapacitance effect and the complementary operating potential windows of ruthenium oxide and MXene. These findings imply that the carbon-based components in asymmetric electrochemical capacitors can be substituted for pseudocapacitive MXene negative electrodes, which will increase their energy density. MXenes can also be utilized as a conductive substrate for oxide growth, which helps to enhance the performance of supercapacitors by acting as a spacer to prevent the MXene sheets from aggregating during charging and discharging. According to Fig. 5(c), Sree Raj *et al.*[24] prepared VTe$_2$/MXene heterostructures for supercapacitor electrode materials by growing vanadium telluride in MXene *via* solvothermal conversion, and synergistically induced interaction effects increased the capacity of the heterostructures up to 250 F g^{-1} with excellent cycling stability. Furthermore, MXene-induced enhancement of the electronic Te 5p states close to the Fermi energy level was predicted to improve the performance of the VTe$_2$/Ti$_3$C$_2$ hybrids in supercapacitor applications by density-functional theory calculations. Moreover, the TM increased the interfacial contact between the MXene flakes, which helped to provide short diffusion ion channels. As illustrated in Fig. 5(e)–(g), Yang *et al.*[31] used a pristine Ti$_3$C$_2$T$_x$ aerogel as a porous structure template that is well preserved during the ALD preparation process, which effectively increased the ion/electron transport pathways and exposed more active sites.

This resulted in a 3D porous MoS_2/MXene hybrid aerogel structure with a conformal heterogeneous interface. Meanwhile, based on the conformal ALD deposition of MoS_2 with a controllable thickness on the porous surface of the MXene template, a substantial amount of heterogeneous interfaces between MoS_2 and $Ti_3C_2T_x$ was created, and furthermore the multiplicity performance and cycling stability of the electrode could both be considerably improved by this heterogeneous structure, which has the capacity to work in concert.

3. Designing porous TM-based architectures for supercapacitor applications

Different strategies can be used to easily design and fabricate ordered, disordered, and layered TM-based porous nano-architectures by investigating them in terms of size, pore structure, and surface chemical properties. In this section, we systematically summarize the latest research advancements in TM oxides, hydroxides, sulfides, phosphides, carbides, and other compounds used as supercapacitor electrode materials, and illustrate and compare their design purpose, synthetic process, structural feature, and electrochemical energy storage performances.

3.1 Porous TM oxide-based electrodes

Typical porous TM oxides have high thermal and chemical stability, flexible surface chemistry and structure, and abundant oxygen vacancies/defects.[136] Numerous TM oxides have been successfully prepared with a porous morphology and different compositions, components, crystalline phases, and pore size distributions, including Co_3O_4, NiO, Fe_2O_3, MnO_2, WO_3, MoO_3, and TiO_2, as well as mixed TM oxides.[137] However, despite their many excellent properties, the practical application of TM oxides in supercapacitors remains relatively limited. This is mainly due to their sustained Faraday reaction, which can lead to significant structural changes or disruptions, as well as phase transitions during cycling, leading to a decrease in their capacitive performance over time. This chapter summarises a number of new synthetic approaches that can provide stable porous structures, controlled phases and effective control over the size of the metal oxides, thereby improving their performance in supercapacitor applications. Table 1 summarizes some typical TM oxides, including their morphology, specific capacitance, and long cycle stability.

Cobalt oxide is a common TM oxide that has attracted great interest in supercapacitor electrode applications due to its high theoretical capacity of 3560 F g^{-1}, high cycling stability, and controllable structural morphology.[138] Benefiting from the tunable structure of cobalt oxides, various microtopographies of Co_3O_4 have been reported, such as nanosheet arrays,[139] nanorods,[140] nanoflowers,[141] nanospheres,[142] and nanocubes,[143] and its rich morphology endows it with different energy storage performances. By reducing the mass and charge diffusion distances and producing more active sites due to their small particle size and high surface/volume ratio, nanoscale active

materials can maximize the material utilization and enhance the electrochemical properties. For example, Liu et al.[144] successfully prepared ultrafine Co_3O_4 nanoparticles via solvent-thermal precipitation, and mainly investigated the effect of temperature on the degree of crystallinity and agglomeration of the crystals during the annealing process. Ultimately, annealing at 250 °C produced uniformly dispersed ultrafine Co_3O_4 nanoparticles, which exhibited the maximum specific capacitance of 523 F g^{-1} at a current density of 0.5 A g^{-1}. After 1500 cycles, the samples that were annealed at 350 °C demonstrated high cycling stability, with a capacitance retention of 104.9%. The low conductivity of Co_3O_4, which influences its electron transport during the energy storage process, may be the reason why the charge storage capacity of Co_3O_4 is typically much less than the estimated specific capacitance in studies. In response to this, Yao et al.[145] looked into how the conducting substrate affected the electrochemical performances of Co_3O_4, and at 1 A g^{-1}, the specific capacitance of the Co_3O_4/rGO/NF system reached 1016.4 F g^{-1}. Nevertheless, at the same current density, Co_3O_4/NF without rGO could only generate a specific capacitance of roughly 520 F g^{-1}. At 7 A g^{-1}, Co_3O_4/rGO/NF retained approximately 95.5% of its initial capacitance value after 3000 charge/discharge cycles.

The numerous oxidation states, high reversible capacity, large specific surface area, layered porous structure, and good structural durability of porous nickel oxide and its composites have made them popular choices as supercapacitor electrode materials.[146] Their abundant pores and size distribution enhance the ion/electron transport rate, reduce the distortion during long cycling, and significantly improve their stability. However, although nickel oxide has a theoretical capacity of up to 2584 F g^{-1}, this theoretical capacity remains unrealized due to its low electrical conductivity.[147] Furthermore, nickel oxide has an agglomeration effect, which reduces its exposed active sites. In this case, to achieve a high specific capacitance and long cycle stability, Wu et al.[18] vertically deposited 2D ultrathin porous nickel oxide nanoplatelets on the surface of 3D nickel foam using a solvent thermal technique. More active sites were exposed by the stacked 2D nanosheets, which also improved the ion/electron transport in the electrolyte.

Because of its broad operating voltage window, multiple valence states, and theoretical specific capacitance of 3625 F g^{-1}, Fe_2O_3 is regarded as one of the most potential pseudocapacitor materials for real-world applications, in addition to traditional carbon-based anode materials. However, Fe_2O_3 always exhibits low conductivity and irrecoverable volume expansion during electrochemical reactions, which makes its electrochemical performance fail to meet expectations. Thus, to solve this problem, Fe_2O_3 is usually combined with conductive nanomaterials to improve its electrochemical performance. Wang et al.[148] used a self-sacrificial template and an in situ gas-phase polymerization method to successfully grow hierarchical α-Fe_2O_3/PPy nanoarrays on CC. At 0.5 mA cm^{-2}, the electrode made of T-Fe_2O_3/PPy NAs demonstrated good reversibility and a high area capacitance of 382.4 mF cm^{-2}. Another useful tactic to enhance the electrochemical performance of Fe_2O_3 is the design and construction of distinctive heterostructures. Li

Table 1 Comprehensive summary of the morphology, specific capacitance, and cycling stability of porous TM oxides

TM oxides	Morphology	Specific capacitance	Cycle performance
Co_3O_4 (ref. 150)	Nanosheets	1782 F g^{-1}@1.8 A g^{-1}	90%, 2000 cycles, 10.8 A g^{-1}
Co_3O_4 (ref. 151)	Nanorods	335 mA h g^{-1}@5 A g^{-1}	100%, 100 cycles, 1 A g^{-1}
Co_3O_4 (ref. 141)	Nanoflowers	330 F g^{-1}@0.5 A g^{-1}	100%, 1500 cycles, 2 A g^{-1}
Co_3O_4 (ref. 142)	Nanospheres	523 F g^{-1}@1 A g^{-1}	42.5%, 5000 cycles, 10 A g^{-1}
Co_3O_4 (ref. 143)	Nanocubes	1913 F g^{-1}@8 A g^{-1}	70%, 650 cycles, 8 A g^{-1}
NiO (ref. 152)	Hierarchical mesoporous	3114 F g^{-1}@5 mA cm^{-2}	87.6%, 4000 cycles, 30 mA cm^{-2}
NiO (ref. 153)	Nanosheets	1169 F g^{-1}@1 A g^{-1}	92.9%, 5000 cycles, 8 A g^{-1}
G@NiO (ref. 154)	Nanosheets	1073 C g^{-1}@1 A g^{-1}	99%, 10 000 cycles, 10 A g^{-1}
Fe_2O_3 (ref. 155)	Nanocubes	1687 mF cm^{-2}@2 mA cm^{-2}	95.8%, 20 000 cycles, 100 mV s^{-1}
Fe_2O_3/PPy (ref. 148)	Nanoarrays	382.4 mF cm^{-2}@0.5 mA cm^{-2}	97.2%, 5000 cycles, 100 mV s^{-1}
MnO_2 (ref. 156)	Nanosheets	417.5 F g^{-1}@1 A g^{-1}	100%, 10 000 cycles, 1 A g^{-1}
MnO_2/CNT (ref. 157)	Nanoarrays	2579 mF cm^{-2}@1 mA cm^{-2}	90%, 5000 cycles, 100 mV s^{-1}
WO_3 (ref. 158)	Nanoflowers	196 F g^{-1}@10 mV s^{-1}	85%, 5000 cycles, 100 mV s^{-1}
WO_3 & V_2O_5 (ref. 159)	Thin film	40.28 F cm^{-2}@0.1 mA cm^{-2}	92.5%, 50 000 cycles, 100 mV s^{-1}
MoO_3 (ref. 160)	Nanosheets	829 F g^{-1}@2 A g^{-1}	91%, 2000 cycles, 2 A g^{-1}
S-MoO_3 (ref. 161)	Nanorods	6.19 F cm^{-2}@0.5 mA cm^{-2}	90%, 5000 cycles, 100 mV s^{-1}
TiO_2 (ref. 162)	Nanotube	3.8 mF cm^{-2}@25 μA cm^{-2}	92%, 20 000 cycles, 100 mV s^{-1}
PANI/TiO_2 (ref. 163)	Nanotube	897.35 F g^{-1}@0.2 A g^{-1}	86.2%, 1500 cycles, 1 A g^{-1}

et al.[149] proposed a core-branch hybrid nanostructure by integrating Fe_2O_3 nanopins (NiNTAs@Fe_2O_3 nanopins) on an array of ultrafine nickel nanotubes. Ultrafine nickel nanotubes were formed through an enhanced template-assisted method in a synthetic process that follows a bottom-up approach. In an aqueous electrolyte, the asymmetric supercapacitor composed of NiNTAs@MnO_2 nanosheet cathode exhibited the maximum energy density of 3197.7 W kg^{-1} because of its specially designed structure with efficient electron transport paths and short ion diffusion paths. Because of its exceptional theoretical specific capacitance, excellent cycling stability, and large specific surface area, MnO_2 is also a promising electrode material. However, improving its charge transfer rate is severely hampered by its low electrical conductivity and poor ion transport capacity. Thus, to address this issue, optimizing the electronic structure of MnO_2 has attracted significant interest. More specifically, the electrical structure and charge diffusion kinetics of TM oxides are typically greatly influenced by the local coordination environment of the TM atoms, which includes their oxidation state, coordination number, and coordination structure. Using TEA as a common complexing agent, Zhang *et al.*[156] accomplished the successful preparation of MnO_2-TEA nanosheets *via* solution chemical deposition. More oxygen vacancies were formed by appropriately adjusting the coordination environment of the manganese atoms in MnO_2-TEA. In the meantime, the electronic structure of MnO_2-TEA was effectively altered by the optimized coordination environment of the manganese atoms, as demonstrated by DFT calculations and Bader charge analysis, greatly enhancing the electrical conductivity and ion diffusion capacity of the material. The prepared MnO_2-TEA exhibited a higher capacity of 417.5 F g^{-1} at 1 A g^{-1}. Then, the only way to achieve the high capacity of MnO_2 is to create low-dimensional, low-loading nanoparticles. Because MnO_2 has inherently low conductivity, the specific capacitance drops sharply when its loading is increased to a critical value of about 10 μg cm^{-2}. This specific capacitance

can only be retained below 30% of the theoretical value. Owing to the constraints at the interface between manganese dioxide and the conductor, doping techniques can enhance the electrochemical performances of MnO_2 by enhancing its electrical conductivity. For instance, Kang *et al.*[164] utilized nonequilibrium doping of metal atoms possessing free electrons (*e.g.*, Au, Ag, and Cu) to improve the conductivity of a thick MnO_2 film, and the doped metal atoms could change the electronic structure of MnO_2, leading to an improved capacitance performance and conductivity. The resultant thick film, Au-doped MnO_2, exhibited outstanding cycling stability and a very high specific capacitance. Mixed TM oxides with two different cations have great potential for electrode applications in supercapacitors.[11] These electrode materials are extremely electrochemically active due to their complex chemical composition, abundant redox active sites, fast electronic transmission channels, and synergistic effects between different species. According to Fig. 6(a–e), Qiu *et al.*[11] used a hydrothermal process to grow $ZnCo_2O_4$/MnO_2 nanosheets with a large surface area and a mesoporous, core–shell structure on 3D nickel foam. The prepared composites possessed a good mesoporous structure with interconnected conductive network. Consequently, an excellent specific capacitance of 2339 F g^{-1} and 1526 F g^{-1} at 1 A g^{-1} and 10 A g^{-1}, respectively, was demonstrated by this specially structured electrode material. By using template-assisted electrodeposition, Liu *et al.*[165] created a hierarchical nanotube array on carbon fibre cloth, which had a high specific capacitance of 2200 F g^{-1} at 5 A g^{-1} and retained 98% of its initial capacitance after 5000 cycles. This array featured a large number of layered tops and discrete separated core–shell structured nanotubes, or nickel–cobalt metal cores. An additional essential oxide is MTMOs, which have the general formula ABO_3, where A and B are rare-earth metals and TM, respectively.[166] Binder-free NiO/$LaNiO_3$ thin-film electrodes were prepared by Liu *et al.*[167] using a spin-coating technique. The NiO/LNO electrodes with the
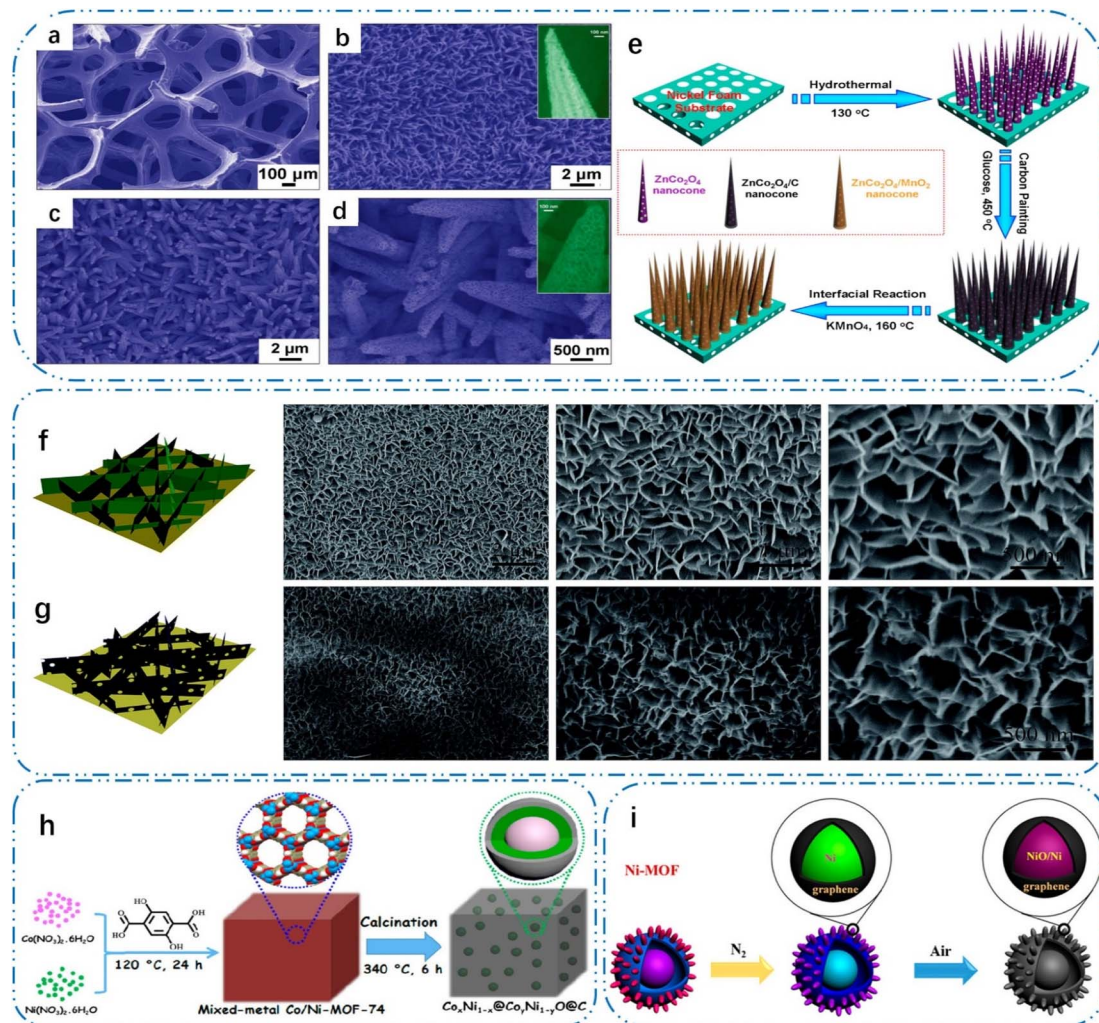
Fig. 6 SEM images of (a) Ni foam; (b) $ZnCo_2O_4$ NCFs (and a magnified view in inset); (c) and (d) $ZnCo_2O_4/MnO_2$ NCFs taken at different magnifications. (e) Schematic illustration of the fabrication processes of $ZnCo_2O_4/MnO_2$ composite nanocone forests (NCFs) with a hierarchical core/shell structure, reproduced from ref. 11 with permission from [Elsevier], Copyright [2015]. Schematic illustration and SEM images of (f) ultrathin $Ni_3(NO_3)_2(OH)_4$ nanoflakes and (g) ultrathin porous NiO nanoflakes on nickel foam at different magnifications, reproduced from ref. 18 with permission from [the Royal Society of Chemistry], Copyright [2016]. (h) Illustration of the synthetic scheme for $Co_xNi_{1-x}@Co_yNi_{1-y}O@C$, reproduced from ref. 30 with permission from [the American Chemical Society], Copyright [2017]. (i) Schematic illustration of the formation of NiO/Ni/graphene composites, reproduced from ref. 37 with permission from [the American Chemical Society], Copyright [2016].

appropriate LNO content demonstrated a good cycling performance and a high specific capacitance.

MOF-derived TM oxides are promising materials for many applications, particularly as electrodes for supercapacitors, because the organic ligands of MOFs are rich in oxygen-containing groups and their derivatives can well retain the porosity and functionality of MOFs.[168] The stability of many MOF-derived TM oxides, ranging from basic 3D oxides to intricate perovskites, is attributed to the high activity of oxygen. Various modifications of TM oxides, as well as composites, have been carried out by selecting suitable strategies for MOF precursors, including a selection of metals, doping, temperature, defects, and other variables. During the conversion of MOFs to TM oxides, oxygen is introduced through several strategies, as follows: (1) attachment to the chemical groups of the MOF organic ligands; (2) introduction through gases during

thermal conversion; and (3) ions from the solvent during solvent thermal conversion. Given that most organic ligands contain oxygen ligands and oxygen is abundant in the air, the strategy of MOF derivatization to TM oxides is easy. Given that most MOFs contain oxygen ligands in their organic ligands and are oxygen-rich in air, MOF derivatization to TM oxides is a very easy strategy. Furthermore, most of the metal ions and organic ligands in MOFs are joined by carboxylic acid groups, and thermal degradation results in the production of derivatives rich in TM oxides. Although thermal decomposition is sufficient to oxidize the metal completely, carbon also reacts with oxygen to reduce the metal. One solution is to increase the conversion temperature in an inert gas to increase the oxidation within the metal, but this process also causes the oxidation of the composite to decrease. According to Fig. 6(h), Sun *et al.*[30] utilized nickel-based MOF-74 to thermally convert to carbon-

covered Ni/NiO under N_2. It was found that Ni was fully oxidized at ≥ 550 °C. Subsequently, the oxidation of the composite was reduced by the thermal decomposition of the nickel-based MOF-74 at ≥ 550 °C. Next, the thermal conversion of the MOF-74, which is based on nickel, under a nitrogen atmosphere completely oxidized the composite. After adding Co to Ni-based MOF-74, it was discovered that the oxidation state of Ni remained unchanged.

However, when both Ni and Co were added during the synthesis of the MOF, Ni and Co were not fully oxidized. This suggests that either Ni and Co enhance the oxidation resistance or Co is oxidized at a higher priority than Ni, resulting in the formation of an oxide layer. Even at transformation temperatures as high as 900 °C, Razaee et al.[169] showed that metallic nickel and cobalt were present in MOF-derived carbon composites. The presence of metallic nickel and cobalt in MOF-derived carbon composites was demonstrated by Razaee et al.[169] The MOF precursor produced by the former, in contrast to the study conducted by Sun et al.,[30] did not contain the two hydroxyl groups present in the ligand utilized by the latter. These findings highlight the significance of the oxygen content in the MOF ligands, which causes the TM oxides to oxidize internally. Also, this emphasizes the importance of choosing the appropriate organic ligand in the synthesis of MOFs, and when using multiple ligands, their ability to regulate the degree of oxidation should also be considered. This also provides ideas for improving the antioxidant properties of MOF derivatives. Firstly, MOFs can be synthesized by choosing organic ligands with a low or even no oxygen content to reduce the oxidation degree of MOF derivatives. Besides, the pyrolysis temperature can be lowered to reduce the degree of oxidation.

Thermal conversion in air for the preparation of TM oxides is one of the most common strategies due to the abundance of oxygen in the air. However, the high activity of oxygen enhances the bonding between ions, causing the MOF to undergo agglomeration. Thus, to avoid this, the temperature during the reaction is usually lowered. Wu et al.[170] created Co_3O_4 nanorods, which had a high surface area of 124 m^2 g^{-1}, by thermally converting Co-MIM nanorods for 30 min at 400 °C. At lower temperatures, the degree of TM oxide crystallization diminished. Another strategy is to use pyrolysis to prevent the oxidation of carbon, and internal oxidation is not as good given that it needs to be replenished by oxygen from the air. Therefore, when an MOF forms TM oxides with little structural change, its original morphology is preserved to the greatest extent, and the degree of crystallization in the TM oxides is maximized by using a multi-step transformation. Pan et al.[171] pyrolyzed ZIF-8 at 350 °C, and then thermally transformed it to ZnO at 400 °C. The original pyrolysis kept 'the morphology of ZIF-8 intact, and thermally changed ZnO crystallized more intensely after that. ZnO crystallized to a higher degree, making it less likely to agglomerate. A two-step selective oxidation is used to prepare TM oxides when in situ oxygen is needed and carbon must be retained. Similar to the multi-part conversion strategy, the carbon and MOF morphology are preserved by first pyrolyzing the MOF precursor. Subsequently, the carbon-derived carbon composite is oxidized in air at lower

temperatures (<350 °C), but during this process, the carbon is not oxidized. This has been demonstrated for the Co_3O_4-carbon composites prepared by Guan et al.[172] This method worked well for creating other TM oxide–carbon composites as well because it allowed partial oxidation to be accomplished by stopping the oxidation process in the second step earlier.[37]

The solvent thermal conversion method for the preparation of TM oxides, although not common, has some advantages due to its lower conversion temperature. The lower temperature minimizes the agglomeration effect[173] that occurs during MOF conversion. Fig. 6(i) demonstrates the synthesis of Ni-MOF with a unique hierarchical hollow-sphere nanostructure by solvothermal reaction. Hierarchical NiO/Ni nanocrystals covered with graphene shells were obtained after successive carbonisation and oxidation treatments with the sphere-in-sphere nanostructures remaining intact in the hollow spheres, although the thermal conversion of other MOF derivatives is constrained by the range of feasible reactant bases (carboxylate, acetate, etc.).[173]

3.2   Porous TM hydroxide-based electrodes

TM hydroxides are some of the essential elements to solve the problem of low energy density of supercapacitors due to their strong mechanical properties, stable physical and chemical properties, flexible surface chemistry and interfaces, and abundant oxygen vacancies due to their high redox activity.[174] However, TM hydroxides have problems that restrict their broad application, including low electrical conductivity and morphological damage from the swelling and shrinking of the electrode during charging and discharging.[175] There are two basic approaches to address these issues, where the first involves compounding TM hydroxides with conductive materials to quicken the reaction kinetics, and the second involves creating porous nanostructures that can efficiently absorb the stresses caused by the expansion and contraction of the electrode.[176] A promising electrode material for supercapacitors is nickel hydroxide, which has an extremely high theoretical capacity of 3650 F g^{-1}. Because of its loose crystal structure, which makes ion insertion and extraction simple and $Ni(OH)_2$ hydration favorable for electrochemical reactions, this material demonstrated an impressive capacity. Unfortunately, the poor electrical conductivity of $Ni(OH)_2$ leads to subpar electrochemical performances; alternatively, $Ni(OH)_2$ composites with carbon matrix show good reproducible and cycling properties. Wang et al.[177] utilized a graphene composite with $Ni(OH)_2$, which exhibited a high capacity of 1335 F g^{-1} at 2.8 A g^{-1} and a reproducible performance of 953 F g^{-1} at 45.7 A g^{-1}. Furthermore, $Co(OH)_2$ has garnered significant interest owing to its comparable characteristics and elevated capacity in comparison to $Ni(OH)_2$. Gao et al.[178] fabricated a pseudocapacitive electrode with high capacitance performance by combining rationally designed $Co(OH)_2$@FeCo hydroxide with an enhanced specific capacitance and reproducible performance and carbon composite material as the cathode and anode. High capacitance performance asymmetric supercapacitors were created, offering a high energy density of 64.1 W h kg^{-1}, power

density of 15 kW kg^{-1}, and robust cycling capability. Nevertheless, $Co(OH)_2$ and $Ni(OH)_2$ share a similar disadvantage in that their practical applications are limited by their low potential window. TM hydroxides exhibit a high-capacity performance at low mass loadings of active materials, while obtaining high-capacity performance at a high mass loading remains a great challenge. Thus, the rational design of the electrode microstructure is necessary to maximize the capacity at a high mass loading. Additionally, the multi-synergistic metal effect can effectively increase the energy density of the electrodes. A nickel–cobalt hydroxide composite with a 3D porous structure was described by Gao et al.[179] The pore sizes in the hierarchical structure were systematically tuned to provide a high capacity at a mass loading of 230 mg cm^{-2}. Active sites and structural rearrangements were triggered by an in situ electrochemical activation method.

Layered double hydroxide (LDH) is considered to be a TM-based electrode with great potential for application due to its relatively high redox activity, rich chemical composition and effective utilization of uniformly distributed TM atoms.[180] Crucially, their intriguing electrochemical properties are also derived from their ease of cation adjustment and anion exchange in their layers without changing their structure. The introduction of metal cations and MOF in the solvent for solvothermal conversion typically yields LDHs, which are then used to prepare non-carbonated MOF derivatives. The conversion process involved is not well studied at the moment because the mechanism involved in the conversion is too complex, but the use of in situ characterization techniques suggests that two interacting processes are involved. The decomposition of the MOF is the first, which is weakened by the metal ions being absorbed from the outside inward.[181] The second involves reassembling LDH crystals from the decomposed MOF. Given that the process of decomposition and reconstruction occurs instantaneously, LDHs are built as a stack of 2D forms of MOFs. These two simultaneous processes can be regulated by changing the salt concentration to control the MOF morphology. Furthermore, the decomposition of MOFs in aqueous solution also has the potential to generate LDHs. As illustrated in Fig. 7(a)–(d), Zhang et al.[8] achieved the thermal conversion of MIL-88A (Fe) in an aqueous nickel-rich ethanol solution by varying the volume ratio of ethanol to water, thereby slowing down the rate of the solvothermal conversion and converting the 3D MOFs into multilayer 2D structures. Besides, LDHs can also be grown directly on substrates. According to Fig. 7(e)–(h), magneto-electrodeposition at high magnetic fields was developed by Li et al.[19] to prepare NiCo-functionalized LDH-CC on CC and MXene. The loading mass and the exposure of active sites were markedly increased because of the magnetic field and the magnetohydrodynamic effect brought on by the electric field coupling. Additionally, 3D cross-linked nested microstructures were built. The fabricated flexible hybrid supercapacitors demonstrated exceptional energy density and cycling stability, and NiCo-LDH offered a high area capacity of 3.12 C cm^{-2} at 1 mA cm^{-2}. Flexible asymmetric supercapacitors based on rGO and CoAl-LDH electrodes were successfully fabricated by Li et al.[182] A simple hydrothermal process was used to grow CoAl-LDH nanosheet arrays directly on CC to create the CoAl-LDH electrode, which had a high specific capacitance of 616.9 F g^{-1} at 1 A g^{-1}. In the end, the hybrid supercapacitors offered a broad voltage range, a high energy density of 0.71 mW h cm^{-2} at 17.05 mW, and a high surface capacitance of 1.77 F cm^{-2} at 2 mA cm^{-2}.

3.3 Porous TM sulfide-based electrodes

TM sulfides have superior electrical conductivity, various oxidation states, and high theoretical capacity compared to TM oxides, and sulfides have superior redox activity compared to carbon-based nanomaterials.[183] These electrochemical properties originate from the redox reactions on the surface of TM sulfides in an electric field, which can counteract the effects of conditions such as potential and electrolyte. However, their small specific surface area and slow ion/electron diffusion rate limit their application in electrochemical energy storage devices.[184] Table 2 summarizes some typical TM sulfides, including their morphology, specific capacitance and cycling stability.

Due to their high electrical conductivity and electrochemical activity, cobalt sulfides with various stoichiometric compositions have gained increasing attention.[185] Chen et al.[186] prepared hierarchical arrays of CoS_2 nanosheets coated directly on a conductive carbon cloth by modulating a thixotropic agent with mutagenic activity. The nanosheets possessed a unique macroporous–mesoporous–microporous structure, which provided multiple-stage channels for the quick diffusion of ions and many peripheral sites for nanoparticles, which is conducive to enhancing the pseudocapacitive effect. The electrochemical characterization results and testing demonstrated that the assembled supercapacitor produced a high energy density of 3.16 mW h cm^{-3} and a high-power density of 1.61 W cm^{-1}, effectively accelerating ion diffusion. Besides, more defects can be constructed with the exchange reaction during pretreatment. By substituting S^{2-} for $Fe(CN)_6^{3-}$ in Prussian blue analogues through an ion-exchange reaction, Cai et al.[187] created oxygen-containing amorphous cobalt sulfide porous nanocubes. A porous structure made up of numerous defect sites was produced by the exchange reaction of anions, and the Co_3S_4 nanocubes also exhibited high electrochemical reactivity. Wang et al.[188] prepared amorphous surface amorphous Co_3S_4 porous flower-like structures using the solvent thermal conversion route, and their defect-rich amorphous surface was demonstrated by using characterization techniques, which enhanced the ionic/electronic transport pathways and accelerated the rate of charge transport within the crystal, increasing the overall electrical conductivity. MoS_2 is a layered TM sulfides in which van der Waals force interactions bind adjacent layers and Mo–S is covalently bonded.[189] As shown in Fig. 8(a), molybdenum sulfides films were used by Ghosh et al.[1] to grow molybdenum disulfide at three distinct temperatures to examine the impact of the growth temperature on surface morphology, film thickness and quality.

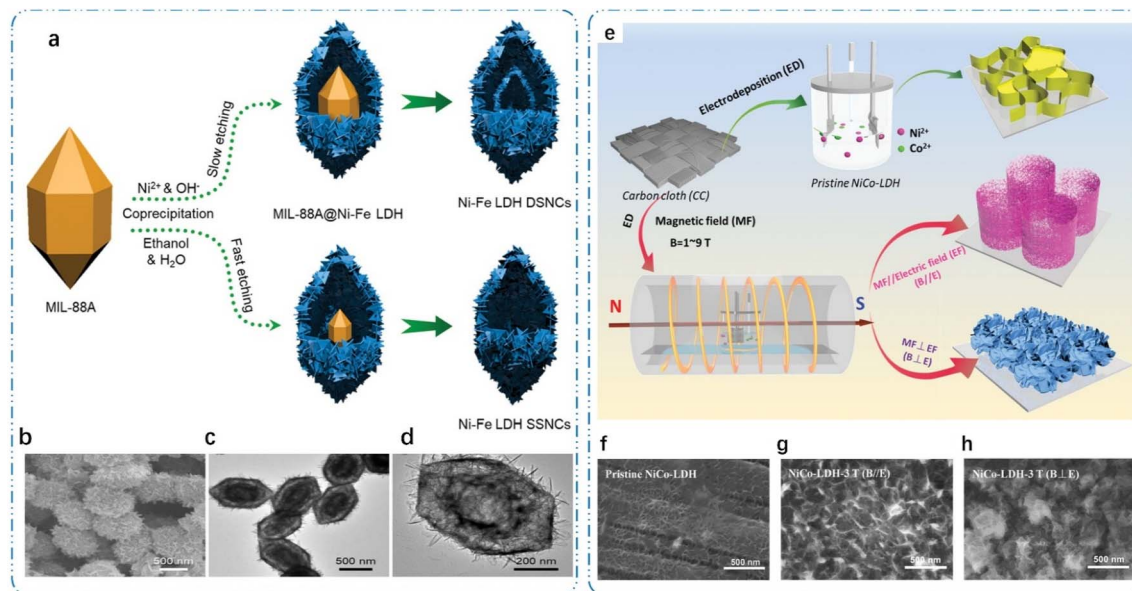Temperature had a considerable effect on the surface morphology, thickness, and microcrystalline size of MoS_2,

Fig. 7 (a) Schematic illustration of the formation of Ni−Fe LDH nanocages with tunable shells *via* a self-templated strategy. (b) FESEM and (c) and (d) TEM images of Ni−Fe LDH DSNCs, reproduced from ref. 8 with permission from [Wiley], Copyright [2020]. (e) Schematic illustration of the preparation of NiCo-LDH on CC. SEM images of (f) pristine NiCo-LDH, (g) NiCo-LDH-3 T (B//E), and (h) NiCo-LDH-3T (B⊥E), reproduced from ref. 19 with permission from [Wiley], Copyright [2022].

despite the material being successfully grown at various temperatures. This study contributes to realizing MoS_2 growth at high throughput in supercapacitor applications. However, the main problems faced by MoS_2 are its structural instability, low conductivity and high internal resistance. Thus, to address these issues, Chen *et al.*[190] created hierarchical MoS_2 nanotube structures that were wired from within CNTs. These CNT-wired MoS_2 nanotube structures offer ultra-high specific capacity, excellent rate capability, and long cycle life because of their unique structural and compositional properties. Due to their superior redox activity, multi-component TM sulfides have much higher electrochemical performance than single-component sulfides. Moreover, the electrical conductivity of poly-TM sulfides is higher than that of their corresponding oxides. In their systematic summary of mixed TM sulfides for electrochemical energy storage, Yu *et al.*[191] discovered that

richer redox reactions and increased electronic conductivity were responsible for the enhanced performance. Additionally, Mohammadi *et al.*[192] described a simple template-mediated assembly technique for creating nanoporous $CuCo_2S_4$ microspheres, which greatly enhanced the conductivity and surface active sites. They exhibited high capacity and durability in supercapacitors, maintaining 95.7% capacity after 5000 cycles.

MOF-derived TM sulfides and oxides share a similar scope of study, but MOF-derived TM sulfides mainly focus on optimizing surface area and activity. Due to the volume expansion during cycling and low electron transfer efficiency, MOF-derived TM sulfides are usually integrated with conductive materials. The strategy of MOF derivatization to TM sulfides is similar to that of TM oxides, and there are three options for introducing sulfur, as follows: (1) chemical groups in the organic ligand of the MOF, such as sulfonates; (2) introduction through gas form

Table 2 Comprehensive summary of the morphology, specific capacitance, and cycling stability of porous TM sulfides

TM sulfides	Morphology	Specific capacitance	Cycle performance
CoS_2 (ref. 186)	Nanosheets	1.29 F cm^{-2}@3 mA cm^{-2}	93.8%, 8000 cycles, 5 mA cm^{-2}
CoS_2@gC/rGO (ref. 198)	Nanocubes	233 F g^{-1}@1.5 A g^{-1}	75%, 5000 cycles, 20 A g^{-1}
Co_3S_4 (ref. 188)	Nanoflowers	1043.9 F g^{-1}@0.5 A g^{-1}	100%, 10 000 cycles, 2 A g^{-1}
MoS_2 (ref. 199)	Films	8 mF cm^{-2}@10 mV s^{-1}	92%, 1000 cycles, 0.22 A m^{-2}
MoS_2 (ref. 200)	Quantum sheets	140 F g^{-1}@5 mV s^{-1}	84%, 5000 cycles, 7.5 mA cm^{-2}
MoS_2/CNT (ref. 201)	Nanosheets	267 F g^{-1}@2 A g^{-1}	90%, 2000 cycles, 5 A g^{-1}
O-MoS_2 (ref. 202)	Nanospheres	744.2 F g^{-1}@1 A g^{-1}	77.8%, 10 000 cycles, 5 A g^{-1}
$CoNi_2S_4$ (ref. 203)	Nanocages	1890 F g^{-1}@4 A g^{-1}	71.6%, 5000 cycles, 8 A g^{-1}
$CoNi_2S_4$/CNT (ref. 204)	Nanotubes	1530 F g^{-1}@1 A g^{-1}	97%, 10 000 cycles, 2 A g^{-1}
Ni_3S_2//$CoNi_2S_4$ (ref. 205)	Nanoflowers	1291 F g^{-1}@50 mA cm^{-2}	91%, 2000 cycles, 100 mV s^{-1}
$NiCo_2S_4$ (ref. 206)	Nanoflowers	2036.5 F g^{-1}@1 A g^{-1}	94%, 5000 cycles, 50 A g^{-1}
$CuCo_2S_4$ (ref. 207)	Nanosheets	1064.5 F g^{-1}@1 A g^{-1}	81.2%, 5000 cycles, 20 A g^{-1}

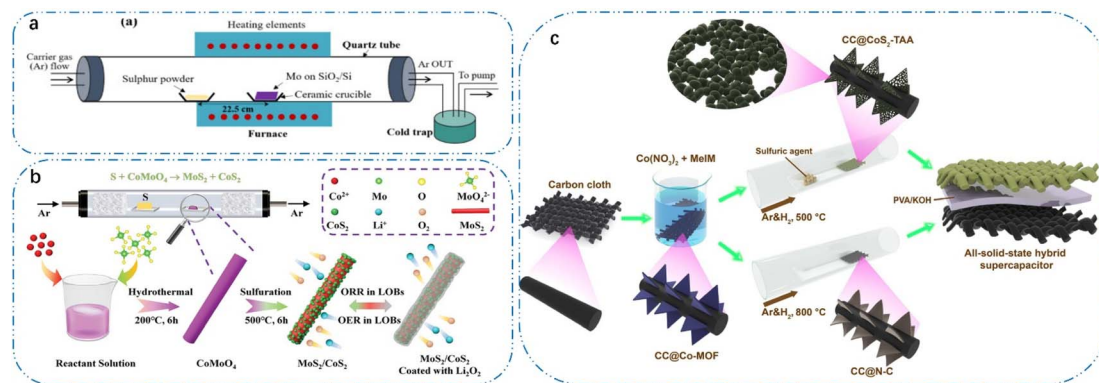© 2024 The Author(s). Published by the Royal Society of Chemistry

Fig. 8 (a) Schematic diagram of the growth chamber, reproduced from ref. 1 with permission from [Elsevier], Copyright [2020]. (b) Schematic illustration of the synthesis of MoS_2/CoS_2 with the proposed lithium storage mechanism, reproduced from ref. 8 with permission from [Wiley], Copyright [2022]. (c) Schematic illustration of "two from one" strategy for fabricating the CC@CoS₂-TAA cathode and CC@N−C anode followed by assembling them into a flexible all–solid–state HSC, reproduced from ref. 15 with permission from [Elsevier], Copyright [2021].

during the thermal conversion process; and (3) introduction through the ionic form in the solvent thermal conversion process. Given that sulfides share the same high activity as oxides, they have been studied equally extensively.

Unlike carboxylate-based ligands, sulfonate-based ligands containing sulfur are limited in MOF but are also sufficient to provide an adequate source of sulfur during the conversion of MOF to TM sulfides. As shown in Fig. 8(b), MOF precursors were prepared by Chen *et al.*[193] using six different metals, and then they were pyrolyzed with both sulfur-containing and non-sulfur-containing ligands to yield TM sulfides. The molar ratio of TM to sulfur in the MOF was unchanged, but after conversion to TM sulfides, it changed. This indicates that the metal has variable reactivity with sulfur in TM sulfides. However, there are also many uncertainties, which hinder the development of MOF-derived TM sulfides. The use of sulfur-containing powder evaporation to thermally convert MOFs to TM sulfides is the most popular strategy. Because of the low cost of sulfur, an excess source of sulfur is typically used to ensure complete conversion, and the conversion process is also doped with carbon, potentially altering the properties. However, this can also lead to the creation of multiphase TM sulfide mixtures. Thus, to avoid this drawback, as illustrated in Fig. 8(c), using MoS_2 nanorods as anchors, Li *et al.*[5] synthesized porous nano-particles of CoS_2. To ensure that impurities such as Co and Co_9S_8 were not generated, the vulcanization process needed to be carefully controlled, which was accomplished by controlling the ratio of evaporated sulfur to the MOF precursor. However, there may be issues with the powder evaporation method of converting MOFs to TM sulfides due to sulfur deposition during cooling and low reactivity of certain TM and S. The low reactivity of certain metals or MOFs containing sulfur, together with the deposition of sulfur in the lower temperature region of the process restrict the gas-phase thermal conversion. Solvent thermal conversion is a good solution to this problem. This method is typically used in a sulfur-ion-containing solution, where the metal ions in MOFs react and degrade into TM sulfides as a result. Given that the temperature of solvent thermal reforming is low compared to gas thermal reforming,

no carbonization occurs, and thus the TM sulfides derived from solvent thermal reforming do not contain carbon. However, the structure of carbon in the vulcanizing agent is stable, and thus it will maintain its form during the conversion process. Therefore, it is possible to prepare MOF-derived carbon composites, and then convert them to TM sulfide–carbon composites using solvent thermal conversion. For the selection of solutions containing sulfur ions, most strategies use TAA. TAA is an organosulfur compound that, at 90 °C, releases reactive sulfur ions and is soluble in ethanol. The use of TAA is generally accomplished in a long thermal conversion time, but the study by Nagaraju *et al.*[15] illustrated that some structures are sensitive to the conversion time and that a short period is not enough for MOFs to be converted to TM sulfides, but a long conversion time can cause the structure to collapse. Currently, many studies have found the optimal transformation time, which makes the solvothermal method the most promising strategy.

3.4 Porous TM phosphide-based electrodes

TM phosphides have attracted increasing attention in the application of supercapacitor electrodes because of their excellent physical–chemical characteristics and wide range of application areas.[194] As illustrated in Fig. 9(b) and (c), numerous TM phosphides, such as Ni_2P, Ni_5P_4, CoP, and FeP, have been effectively explored in various electrochemical energy applications.[23] However, TMP electrode materials usually suffer from slow reaction kinetics and volume expansion, resulting in poor performances and cycling stability. In this case, one useful method for enhancing their electrochemical performances is the synthesis of TM phosphides with porous structures, and porous TM phosphides with a uniform pore size distribution can be realized by controlling their templates, molar ratios of precursor-to-phosphorus source, and thermal conversion temperatures. Table 3 summarizes some typical TM phosphides, including their morphology, specific capacitance, and cycling stability.

In recent years, nickel phosphide has found extensive application in the field of electrochemical energy storage owing
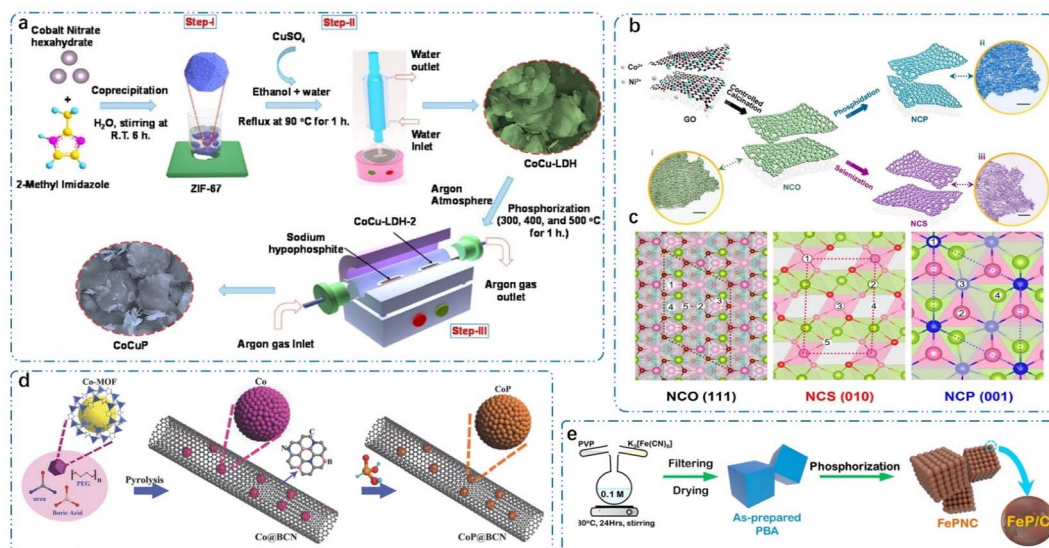
Fig. 9 (a) Graphic elucidating the synthesis process of ZIF-67, CoCu-LDH and the CoCuP composite, reproduced from ref. 3 with permission from [Elsevier], Copyright [2023]. (b) Scheme of the synthesis of NCO, NCS, and NCP holey nanosheets and corresponding STEM images and (c) atomic structure of the hydrogen-covered surface, reproduced from ref. 23 with permission from [the American Chemical Society], Copyright [2018]. (d) Schematic illustration for the fabrication of CoP@BCN nanotubes, reproduced from ref. 28 with permission from [Wiley], Copyright [2017]. (e) Schematic illustration of the synthesis process and formation of the FeP nanocubes derived from as-prepared PBA (FePNC), reproduced from ref. 35 with permission from [Wiley], Copyright [2018].

to its distinct physical and chemical properties.[195] Most of the studies on nickel phosphide have focused on its multi-component or high-throughput preparation strategies, whereas the synthesis of its porous micro–nanostructures has not been widely investigated. Wang et al.[196] prepared $Ni_{12}P_5$ hollow nanorod structures with a typical size of 20 nm and the wall thickness of 3 nm using solvothermal conversion. In addition to excellent activity, $Ni_{12}P_5$ has a higher capacity of 949 $F\,g^{-1}$ at 1 A g^{-1}. When utilized as a supercapacitor electrode, the honeycomb matrix nickel phosphide material created by Jun et al.[197] exhibited a superior electrochemical performance. When sodium hypophosphite is used as a precursor, PH_3 gas can be decomposed at a lower temperature, which is not only good for the complete phosphatization of the precursor, but PH_3 is also a good reducing agent to prevent the precursor from oxidizing during the thermal conversion process. Cobalt phosphides (e.g., CoP and Co_2P) have been increasingly used in electrochemical technology because of their broad stoichiometric composition, reliable stability, low overpotential, and high specific capacitance.[208] As illustrated in Fig. 9(a), by combining catalyst powders with solvents and suitable polymer binders, numerous TM-based electrode materials based on cobalt phosphide have been created, which are subsequently modified on the substrate surface.[209] Currently, it is challenging to tailor the desired pore size distribution on the surface of the materials, which can result in the loss of surface activity. An effective approach to address this issue is electrochemical deposition, which allows for easy control of the composition, size, and distribution of pores in the material. For instance, Kim et al.[114] used electrochemical deposition to create a 3D porous Co–Fe–P foam material. This material is highly active, porous, and has stable cyclic stability in addition to high

Table 3 Comprehensive summary of the morphology, specific capacitance, and cycling stability of porous TM phosphides

TM phosphides	Morphology	Specific capacitance	Cycle performance
Ni_2P (ref. 221)	Nanosheets	2293 $F\,g^{-1}$@1 A g^{-1}	88%, 10 000 cycles, 15 A g^{-1}
CoP (ref. 222)	Nanospheres	723 $F\,g^{-1}$@1 A g^{-1}	94.3%, 50 000 cycles, 30 A g^{-1}
FeP_4 (ref. 223)	Nanocages	345 $F\,g^{-1}$@1 A g^{-1}	89%, 10 000 cycles, 10 A g^{-1}
$Ni_{12}P_5$ (ref. 224)	Nanospheres	955 $F\,g^{-1}$@1 A g^{-1}	81%, 1500 cycles, 5 A g^{-1}
$Ni_{12}P_5$ (ref. 224)	Nanowires	871 $F\,g^{-1}$@1 A g^{-1}	69%, 1500 cycles, 5 A g^{-1}
$Ni_{12}P_5$ (ref. 224)	Nanonets	423 $F\,g^{-1}$@1 A g^{-1}	78%, 1500 cycles, 5 A g^{-1}
Co_2P (ref. 225)	Nanoflowers	416 $F\,g^{-1}$@1 A g^{-1}	97%, 6000 cycles, 1 A g^{-1}
NiCoP (ref. 226)	Nanoflowers	1153 $F\,g^{-1}$@1 A g^{-1}	76.6%, 7000 cycles, 20 A g^{-1}
NiCoMn-P (ref. 227)	Nanorods	1530 $F\,g^{-1}$@1 A g^{-1}	97%, 10 000 cycles, 2 A g^{-1}
CDs/NiFeP (ref. 90)	Nanoflowers	2589 $mF\,cm^{-2}$@2 mA cm^{-2}	88%, 3000 cycles, 20 mA cm^{-2}
NiFe-P (ref. 228)	Nanocubes	793.8 $F\,g^{-1}$@1 A g^{-1}	105%, 5000 cycles, 20 A g^{-1}

electrochemical activity. Most TM phosphides have metal-like properties due to their narrower bandgap, which makes them very promising for supercapacitor electrode applications. Although some MOFs have phosphorus in their organic ligands, few studies have been conducted on converting MOFs to TM phosphides from these phosphorus sources. Moreover, only a few studies have dealt with the conversion of MOFs to TM phosphides using solvothermal conversion. Therefore, most of the strategies for phosphor derivatization of MOFs to TM phosphides are almost exclusively accomplished by thermal conversion in phosphorus gases containing reactive phosphorus or evaporated phosphorus. The easiest strategy for the derivatization of MOFs to TM phosphides is by thermal conversion in evaporated phosphorus gas. Kale *et al.*[3] prepared TM phosphides by phosphorylating ZIF-67 derivatives under reflux at 400 °C, where the phosphorus source was completely evaporated and reacted to form TM phosphides from Co. The process of thermal conversion can be extended by controlling the composition and temperature. Xia *et al.*[210] formed a porous network through *in situ*-generated carbon, allowing Co_xP nanoparticles to be evenly distributed throughout the nitrogen-doped carbon. The factors to be considered in the process of thermal conversion include the raw material molar ratios, granularity, stability of phosphates, temperature range, kinetics of different phosphates, and availability of phosphorus gas. Li *et al.*[211] examined mixed sources of TM and phosphorus, although the majority of research has focused on isolated sources. The investigation involved ball milling RP, dispersing it in an Fe^{3+}-containing solution, combining it with an appropriate ligand to create Fe-MOF gels with dispersed RP, and sublimating RP below its sublimation temperature for pyrolysis to yield $FeP_x@P$. Because the RP is only partially vaporized at these low temperatures, the iron is only partially phosphatized to produce phosphates.[212]

Red phosphorus (RP) is the most commonly used phosphorus source for MOF-derived MP, but sodium hypophosphite (NaH_2PO_2) has two advantages over RP. Firstly, sodium hypophosphite can decompose at lower temperatures to produce phosphine (PH_3) gas, which is easily reacted by MOF to produce TM phosphides.[213] Secondly, as shown in Fig. 9(d), PH_3 is a strong phosphatizing agent at lower temperatures, which makes the conversion of MOF-derived TM phosphides more efficient.[28] Besides, the hydrogen in PH_3 can be used as a reducing agent to remove the oxide layer to increase the reaction efficiency. Kavian *et al.*[214] mixed NiCo-BDC with sodium hypophosphite and pyrolyzed it in argon at 350 °C, producing a small number of nanorods in addition to MOF, a morphology which they suggest may originate from the liquefaction of NaH_2PO_2. However, these liquids can also result in residue-induced microstructural changes and chemical contamination from Na,[35] which reduce the surface area.[215] According to Fig. 9(e), Lim *et al.*[35] designed and prepared porous FeP/C nanostructures *via* the low-temperature phosphorylation of MOF nanostructures. The resulting FeP/C composites had a small pore size distribution and a high specific surface area. They were made of highly porous nanocubes structures with FeP dispersed on carbon scaffolds. In highly ordered MOF-derived nanocubes structures, this particular nanostructure provided abundant reaction sites uniformly distributed, while achieving fast and efficient electron/ion transport.

3.5 Porous TM carbide electrodes

The formation of TM carbides can significantly alter the physicochemical properties of TM.[12] TM carbides are formed by incorporating carbon atoms in the interstitial positions of the TM.[216] In recent years, the construction of nanostructured TM carbides, especially TM carbides with hierarchical porous structures, has made significant progress, and their electrochemical performance has been improved.[20] Because TM carbide electrode materials based on porous structures have more active sites and a larger electrochemically active surface area, they have significant potential application in electrochemical energy storage devices. However, there are still some challenges in the practical application of TM carbons, such as two-dimensional TM carbons with self-stacking phenomenon and poor stability in water–oxygen environment. Currently, researchers have adopted various methods to improve their stability, such as improving the synthesis strategy and adjusting the surface functional groups. This chapter summarises some advanced modification methods in recent years.

In a variety of electrochemical energy fields, nanomaterials based on TM carbides, particularly molybdenum carbide (Mo_2C), have emerged as electrode materials with high electrical conductivity, strong electrochemical activity, and high stability in varying pH electrolytes.[65] Molybdenum carbides have four different crystal structures, which may affect the electrochemical properties of different compositions.[217] Recently, TM carbide nanomaterials with ordered porous structures have attracted an increasing amount of interest in the field of energy storage due to their high active surface area, high dispersion, and large porosity.[218] Huang *et al.*[20] prepared TM carbide nanomaterials of nitrogen-doped carbides *via* thermal decomposition. Nitrogen-doped molybdenum carbide was synthesized by thermal conversion. The porous nanosheets had a reasonable degree of crystal crystallization, and the presence of amorphous carbon could inhibit the material expansion and stabilize the nanosheet structure. Wang *et al.*[219] prepared a nickel-decorated molybdenum carbide hollow structure through gradual dissolution–regeneration, and the nickel-decorated molybdenum carbide presented a higher degree of crystallinity than molybdenum carbide. The nickel-decorated molybdenum carbide possessed higher electrochemical reactivity than molybdenum carbide. Cao *et al.*[65] created layered large dielectric microporous molybdenum carbide with a 3D structure. Because of its special 3D open structure and layered large dielectric microporosity, this material showed excellent cycling stability, strong specific capacity, and magnification capabilities. As an example of TM carbide-based nanoporous structured materials, titanium carbides have good chemical and thermal stability together with high electrical conductivity.[220] Given that the formation of titanium carbide requires activation energy, high-temperature conditions are necessary to prepare titanium carbide. As shown in

Fig. 10(a), Ti_3C_2 is converted to C@TiN by calcination in NH_3. Xu et al.[227] used CVD to create porous TiC/boron-doped diamond composite electrodes, and then they used the plasma electrolytic oxidation (PEO) method to pretreat them. The PEO process resulted in the formation of a porous and nanoscale TiO_2 layer, which inhibited the formation of TiC. During CVD, TiO_2 is reduced with hydrocarbon ions and free radicals to form the TiC phase in situ. Properties such as specific surface area and pore size distribution can be controlled by the reactive ballistic deposition of TiC, which in turn affects the electrochemical performance. Foratirad et al.[228] prepared 2D porous titanium carbide using an etching strategy to exfoliate Ti_3AlC_2 in a hydrogen fluoride solution, with a size of 22.53 $m^2 g^{-1}$. The electrochemical capacity improved with a large capacity of 119.8 $F cm^{-3}$ at 2.5 A g^{-1} due to the large specific surface area of 22.53 $m^2 g^{-1}$. The fast ion/electron transport rate is possible is responsible for the superior electrochemical performance of MXene-based electrode materials. Because titanium carbide MXene can function at a negative potential in an acidic electrolyte, Jiang et al.[16] exploited this property. They combined it with a ruthenium oxide positive electrode to produce a fully pseudocapacitive asymmetric device. The operating voltage window of this asymmetric device was 1.5 V, which is the widest voltage window reported for MXene-based supercapacitors to date and roughly twice that of a symmetric MXene-based supercapacitor. To maximize the energy density of supercapacitors, thicker electrodes are needed for a high-area loading. At the same time, the active material requires a complex, layered pore structure to ensure fast electron and ion transport. To optimize the active material density and guarantee an excellent performance, the porosity and thickness must be balanced. According to Fig. 10(b), Spurling et al.[29] formed hierarchical materials from MXene 2D nanosheets in the form of thin films of interconnected 3D networks, which allowed them to create high-performance thick-film electrodes with well-defined, hierarchical, and porous structures. Although

TM carbides have relatively large particles, they still have electrochemical properties similar to that of platinum group metals.[229] Given that the temperature of solvent thermal conversion is not sufficient for carbonization, MOF thermal conversion is currently a viable method for the preparation of TM carbides.

The organic ligands of MOFs provide the majority of the carbon source for the conversion process. However, after the conversion, the excess carbon is still retained in the TM carbides, resulting in the formation of TM carbides that are primarily carbon composites. Although carbon is contained in the organic ligands of all MOFs, the carbons formed by many metals are not stable, and some metals cannot form carbons at all. At this point it is necessary to use some characterization techniques such as XRD and XPS to determine the bonding and structure.

The bonding of metals and carbon requires high conversion temperatures, usually greater than 600 °C. Furthermore, oxygen can severely hinder the growth of TM carbides, and thus a reducing agent is usually added to the conversion, hydrogen, or a solid that decomposes to produce a reducing agent. As illustrated in Fig. 10(c), Jia et al.[230] successfully synthesized TM carbides by adding H_2 (5 vol%) during thermal conversion, proving the feasibility of the strategy. Kong et al. used solid-state MAE ($C_3H_6N_6$), which underwent gaseous decomposition into N_2, H_2 and CH_4, with nitrogen acting as a dopant and the latter two acting as reductants, to successfully prepare $Co_3InC_{0.75}$ and carbon composites.[231] Among the MOF-derived TM carbides, Mo is by far the easiest element to form TM carbides, which can still be synthesized at lower temperatures even without the addition of reducing agents. Taking advantage of this difference between Mo and other metals, the one-step preparation of TM carbides composites can be achieved, which allows the in situ formation of heterojunctions to maximize the redox active area, and thus improve their performance. However, the dopant of non-metals may also hinder the formation of TM carbides, and
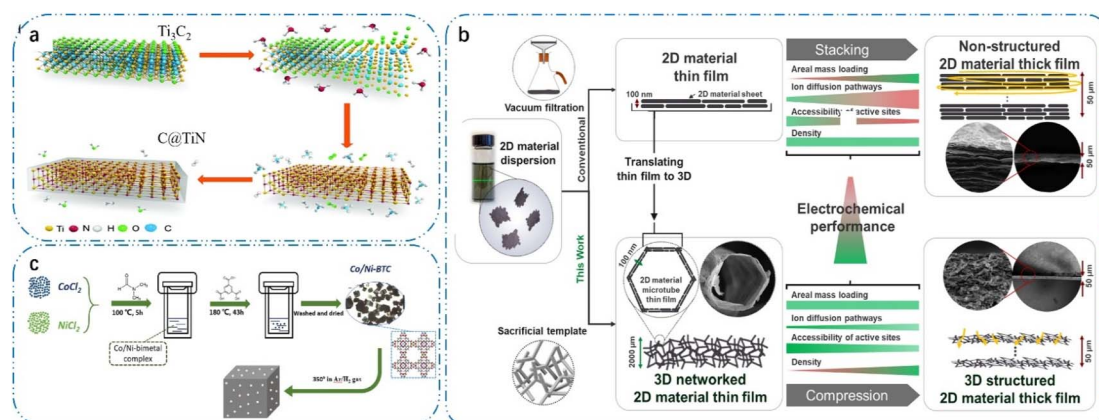
Fig. 10 (a) Schematic of the structural transformation from Ti_3C_2 to C@TiN during calcination at 750 °C in an NH_3 atmosphere, reproduced from ref. 12 with permission from [the Royal Society of Chemistry], Copyright [2018]. (b) Schematic illustration of N@MoPC$_x$, reproduced from ref. 20 with permission from [Wiley], Copyright [2018]. (c) Conventional fabrication method for thick-film electrodes of two-dimensional materials and concepts for thin film fabrication of two-dimensional materials with three-dimensional networking, reproduced from ref. 29 with permission from [Elsevier], Copyright [2024].

therefore limited to TM oxides, TM sulfides, *etc.* paired with it. Although most of the carbon sources for synthesizing TM carbides are provided by MOF organic ligands, carbon composite materials using *in situ* carbon may be insufficient, and thus it is necessary to add *in situ* carbon from carbon additives. However, carbon additives require a high thermal transition temperature, and thus this allows gases such as CH_4 to be used not only as a reducing agent but also as a carbon source. In addition, CH_4 has a lower cracking temperature of only 545 °C, which also reduces the tendency to agglomerate. This makes the synthesis of TM carbides at 600–1600 °C potentially advantageous.

3.6 Porous TM selenide electrodes

TM sulfides are materials with high application potential for supercapacitor electrodes because of their high specific capacitance, but their inadequate stability for cycling, insufficient rate capability, and poor electrical conductivity limit their wide application.[232] Thus, to address the drawbacks of these materials, TM selenides have emerged as a superior substitute.[233] Although selenium has greater electrical conductivity than sulfur and oxygen because of its larger radius and lower ionization energy, it shares similar chemical properties with O and S because it is a member of group VI.[234] Besides, being an abundant material on Earth, triselenides usually display a two-dimensional layered structure akin to graphite, where TM atoms are situated in the space between two layers of selenium.[234] This layered structure suggests a high-rate capability and greater cyclic stability because it allows for the simple and reversible intercalation of other atoms in the interchain gaps, allowing for easy energy storage without structural deformation.[234] Several techniques, including the creation of various porous nanostructures that can increase the active surface area exposed to the electrolyte and encourage ion diffusion, have been developed to enhance the electrochemical performance of TM selenides.[235] According to Fig. 11(a), Shinde *et al.*[7] prepared petal-like NiSe@Cu$_2$Se, where its unique porous structure not only provided more ion/electron transport channels, but also exposed more redox active potentials. Subsequently, rose-nanopetal-like NiSe@Cu$_2$Se. was prepared through an *in situ* conversion reaction, where the FeSe negative electrode was directly immobilized on Cu foam. The excellent electrical conductivity and superior electrochemical properties are linked to the complementary potential windows of the NiCuSe and FeSe electrodes in an aqueous electrolyte. By creating a synergistic effect between the two metal cations, adding additional metals to TM selenides enhances their specific capacitance and gives redox reactions more active sites. Acharya *et al.*[236] used a process employing a zinc–cobalt organic skeleton as a template for self-templating, ion exchange, and selenium to disperse hollow porous nickel–zinc–cobalt selenide nanosheet arrays onto chemically reduced rGO-decorated nickel foams. The Ni–Zn–Co–Se@rGO/NF electrodes offered more electrochemically active sites for the simple insertion of the electrolyte, and the ionic diffusion path was reduced to provide an adequate accessible area, indicating the superior electrochemical performance of the prepared unique porous nanostructures. Furthermore, TM selenides can be hybridized with carbon-based materials such as reduced rGO and CNTs to enhance their charge transfer, electrical conductivity, and cycling life. According to Fig. 11(b)–(g), the creation of CoSe$_2$/C dodecahedra with adjustable internal structures, including solid, yolk–shell, and double-shell configurations, was reported by Zhang *et al.*[17] Cobalt species were utilized as a sacrificial template in the *in situ* reaction with selenium to form CoSe$_2$ nanoparticles using a polyhedral cobalt organic skeleton. Carbon composites with different internal structures could be produced through temperature-controlled annealing in an argon atmosphere, which enabled the controlled preparation of CoSe$_2$. The double-shelled CoSe$_2$/C composites exhibited a good reproducible performance, long cycling stability, and high capacity as an electrode for supercapacitors.

3.7 Other TM-based electrodes

The TM compounds listed herein all have different characteristics, and because of these properties, TM compounds have

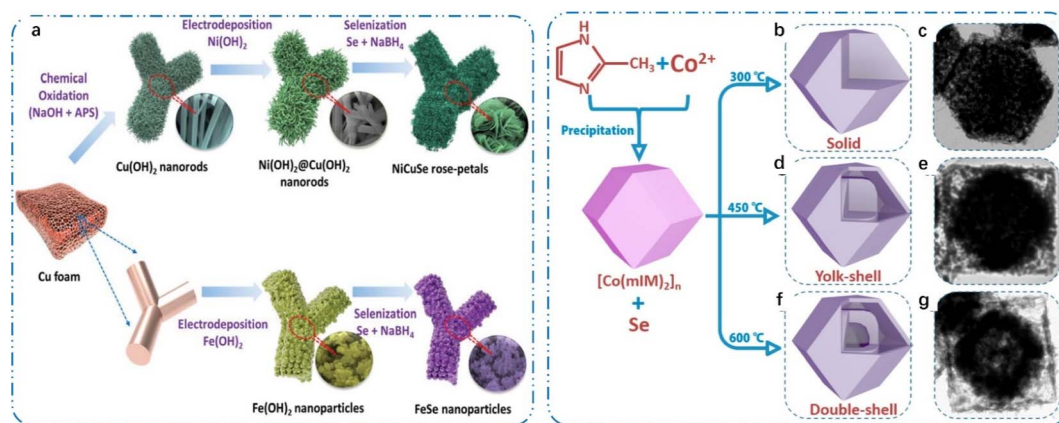**Fig. 11** (a) Schematic illustration of the synthesis procedure of NiCuSe rose-petal structures and FeSe nanoparticles, reproduced from ref. 7 with permission from [Wiley], Copyright [2022]. Schematic illustration of the preparation process of solid (b) and (c), yolk-shelled (d) and (e) and double-shelled (f) and (g) CoSe$_2$/C composite, reproduced from ref. 17 with permission from [Elsevier], Copyright [2017].

abundant applications in supercapacitor electrodes with different energy storage mechanisms. TM oxides have the advantages of high thermal and chemical stability, flexible surface chemistry and structure, and abundant oxygen vacancies/defects, but their intrinsic conductivity is low, and they are not good enough to solve the disadvantage of low energy density of supercapacitors when used as supercapacitor electrode materials. TM hydroxides are one of the keys to solve the problem of low energy density of supercapacitors due to their high redox activity. However, TM hydroxides have the problems of low electrical conductivity and morphological damage caused by the swelling and shrinking of electrode materials during the charging and discharging process. Compared with TM oxides and TM hydroxides, TM sulphides have greater electrical conductivity, mechanical durability and heat resistance, and sulphides have richer redox activity compared with carbon-based nanomaterials. However, their small specific surface area and slow ion/electron diffusion rate limit their application in electrochemical energy storage devices. TM phosphides have a rich phosphide system compared to other compounds, and porous TM phosphides with uniform pore size distribution can be achieved by controlling their templates, precursor-to-phosphorus-source molar ratios, and thermal transition temperatures. However, phosphides, such as oxides, usually suffer from slow reaction kinetics and volume expansion, resulting in poor performances and cycling stability. TM carbides have superior electrical conductivity, and through extensive research they have a rich porous structure. However, compared to other compounds, two-dimensional TM carbons have self-stacking effects and are less stable in aqueous-oxygen environments. Besides the typical TM-based materials mentioned above, other porous TM-based materials have been applied in supercapacitors. This chapter summarizes the strategies for the synthesis of these TM-based electrodes and their application value in supercapacitors.

TM tellurides also typically exhibit properties associated with structural changes due to the larger ionic radii and smaller energy band gaps of TM tellurides,[237] such as $MoTe_2$ films. Similar to selenium, the boiling point of tellurium is much higher than the temperature at which thermal conversion occurs, and thus the reduced air pressure during thermal conversion allows it to be volatilized.[238] For the synthesis of ultrathin $1T'$-$MoTe_2$ nanosheets, Liu et al.[239] devised a colloidal chemical strategy. The obtained samples exhibited a layered extension with an interlayer distance of 0.723 nm and a large number of defects. By altering the Mo precursor and the reaction atmosphere, the shape of $1T'$-$MoTe_2$ could be controlled. CO is essential for characterizing the nanosheets in this reaction. Similarly, TM tellurides can introduce other cations to exert synergistic effects to improve electrochemical properties. The ZnCoTe–N–C anode demonstrated a high specific capacity, where Poudel et al.[240] prepared nanotubes consisting of zinc cobalt telluride-integrated nitrogen-doped carbon and zinc cobalt nanoparticles encapsulating nitrogen-doped carbon. The capacity and stability of the electrode were also improved by the increased electrochemical active sites provided by the graded molybdenum disulfide nanosheets. Consequently, the ZnCoTe-

N-C/MoS_2 electrode displayed superior long-term stability and a greater specific capacity. Furthermore, ZnCo-NPs-N-CNTs had an initial capacity of 207.2 mA h g^{-1}, and even after 50 A g^{-1}, the high specific capacity was retained. The direct growth of redox-rich bimetallic components on the collector prevents volumetric expansion during charging and discharging, which is responsible for the exceptional electrochemical activity of the electrodes. Given that the large ionic radius of tellurides tends to cause swelling of the electrode material, compositing TM tellurides with other materials is also a feasible strategy. The preparation of MOF-derived cobalt telluride–carbon porous structure composites on nickel foam was reported by Kshetri et al.[241] Because of its bifunctional charge storage properties, these composites had an alkaline aqueous solution when used as electrodes in symmetric supercapacitors, with an optimal output voltage of 1.45 V.

4. Conclusions and perspectives

In summary, the porous characteristics of TM-based electrodes endow them with quick electron/ion transport, fast reaction kinetics, and high electrochemical active area, thus efficiently boosting the charge storage performances and rate capacity. Meanwhile, the unique d-electron configuration, multiple oxidation state, and synergistic effect of multi-metals of TM-based electrodes make them competitive candidates for assembling high-performance supercapacitors. The investigation of porous TM-based electrodes characterized by their distinctive structures and characteristics has propelled significant progress in the domain of electrochemical energy storage. The typical synthesis strategies and corresponding conversion mechanism of porous TM-based electrodes were systematically summarized in this review. Additionally, the advancement in crystalline phase, electronic structure, and microstructure evolution for TM-based electrodes as well as their effect on supercapacitor performances were reviewed. These remarkable advances undoubtedly declare the enormous potential for the applications of TM-based electrodes in the domain of supercapacitor energy storage. Among these strategies, the template self-assembly strategy can construct the structure of the product in a controllable manner; the thermal decomposition strategy is widely researched and has a simple preparation process; the chemical deposition strategy makes the porosity more controllable; and the hybridization strategy can effectively improve the inherent shortcomings of TM-based electrode materials. However, there is still much room for development to further improve the electrochemical performance of porous transition metal-based electrode materials and supercapacitors. The following segment delineates many pressing research problems and ongoing challenges that constitute the research priorities that must be considered throughout the forthcoming design and manufacturing processes of superior energy storage components.

Although the processes for creating porous structures have been thoroughly examined, new and advanced methods still need to be discovered and developed. Therefore, to best design these TM-based materials for each unique application, more

methodical theoretical and experimental research is required. More work is specifically required to reduce the number of synthetic attempts and predict the structure–activity relationship by fabricating porous TM-based electrodes with computational assistance.

Various characterization and testing techniques have been developed to demonstrate the formation of porous structures and their size and surface interface relationships. To gain a deeper comprehension of the mechanism of action, and consequently the connection between porous structure and electrochemical performance enhancement, more *in situ* characterization and simulations can be employed. Establishing a clear structure–performance relationship is a challenging task. Creating techniques to measure the energy storage mechanism of specific, well-characterized porous nanostructures can be very beneficial in this regard.

Developing porous materials is essential for enhancing the electrochemical performance of supercapacitors. However, the majority of strategies consistently produce disordered pores, and porosity control still requires work. Thus, to optimize the energy storage performance using strategies such as the engineering of defects, doping with heteroatoms, the addition of multiple pores to the structure (micro, meso, and macro), and other strategies, developing effective, scalable, and controllable processes is crucial for the creation of ordered porous materials. Additionally, the procedures for the preparation of TM-based materials need to be simplified and designed for their low-cost and large-scale production. With the design and development of synthesis strategies and the comprehensive comprehension of structure relationships and energy storage mechanisms, porous TM-based electrode materials will play a greater role in supercapacitor applications.

Author contributions

Feitian Ran, conceptualization, paper writing, and analysis of article structure; Meijie Hu, first draft preparation and error proofreading; Shulin Deng collecting data and error proofreading; Kai Wang, Wanjun Sun, English writing assistant; Hui Peng, Jifei Liu, review and proofreading.

Conflicts of interest

The authors declare no conflicts of interest.

Acknowledgements

Notes and references

1 S. Ghosh, S. S. Withanage, B. Chamlagain, S. I. Khondaker, S. Harish and B. B. Saha, *Energy*, 2020, **203**, 117918.

2 J. X. Feng, S. H. Ye, H. Xu, Y. X. Tong and G. R. Li, *Adv. Mater.*, 2016, **28**, 4698–4703.

3 A. M. Kale, R. Velayutham, A. D. Savariraj, M. Demir and B. C. Kim, *Mater. Today Sustainability*, 2023, **21**, 100335.

4 K. Kang, S. Xie, L. Huang, Y. Han, P. Y. Huang, K. F. Mak, C.-J. Kim, D. Muller and J. Park, *Nature*, 2015, **520**, 656–660.

5 D. Li, L. Zhao, Q. Xia, L. Liu, W. Fang, Y. Liu, Z. Zhou, Y. Long, X. Han, Y. Zhang, J. Wang, Y. Wu and H. Liu, *Small*, 2022, **18**, e2105752.

6 J. Gu, L. Sun, Y. Zhang, Q. Zhang, X. Li, H. Si, Y. Shi, C. Sun, Y. Gong and Y. Zhang, *Chem. Eng. J.*, 2020, **385**, 123454.

7 P. A. Shinde, N. R. Chodankar, M. A. Abdelkareem, S. J. Patil, Y. K. Han, K. Elsaid and A. G. Olabi, *Small*, 2022, **18**, 2200248.

8 J. Zhang, L. Yu, Y. Chen, X. F. Lu, S. Gao and X. W. Lou, *Adv. Mater.*, 2020, **32**, 1906432.

9 X. Zang, C. Shen, E. Kao, R. Warren, R. Zhang, K. S. Teh, J. Zhong, M. Wei, B. Li and Y. Chu, *Adv. Mater.*, 2018, **30**, 1704754.

10 C. Avci, J. Ariñez-Soriano, A. Carné-Sánchez, V. Guillerm, C. Carbonell, I. Imaz and D. Maspoch, *Angew. Chem., Int. Ed.*, 2015, **127**, 14625–14629.

11 K. Qiu, Y. Lu, D. Zhang, J. Cheng, H. Yan, J. Xu, X. Liu, J.-K. Kim and Y. Luo, *Nano Energy*, 2015, **11**, 687–696.

12 W. Yuan, L. Cheng, H. Wu, Y. Zhang, S. Lv and X. Guo, *Chem. Commun.*, 2018, **54**, 2755–2758.

13 S. Wang, J. Qin, T. Meng and M. Cao, *Nano Energy*, 2017, **39**, 626–638.

14 H. Xu, Z. X. Shi, Y. X. Tong and G. R. Li, *Adv. Mater.*, 2018, **30**, 1705442.

15 G. Nagaraju, S. C. Sekhar, B. Ramulu and J. S. Yu, *Energy Storage Mater.*, 2021, **35**, 750–760.

16 Q. Jiang, N. Kurra, M. Alhabeb, Y. Gogotsi and H. N. Alshareef, *Adv. Energy Mater.*, 2018, 1703043.

17 Y. Zhang, A. Pan, Y. Wang, X. Cao, Z. Zhou, T. Zhu, S. Liang and G. Cao, *Energy Storage Mater.*, 2017, **8**, 28–34.

18 S. Wu, K. Hui, K. Hui and K. H. Kim, *J. Mater. Chem. A*, 2016, **4**, 9113–9123.

19 H. Li, S. Lin, H. Li, Z. Wu, Q. Chen, L. Zhu, C. Li, X. Zhu and Y. Sun, *Small Methods*, 2022, **6**, 2101320.

20 Y. Huang, J. Ge, J. Hu, J. Zhang, J. Hao and Y. Wei, *Adv. Energy Mater.*, 2018, **8**, 1701601.

21 J. Tao, R. Tan, L. Xu, J. Zhou, Z. Yao, Y. Lei, P. Chen, Z. Li and J. Z. Ou, *Small Methods*, 2022, **6**, 2200429.

22 B. Kalanyan, W. A. Kimes, R. Beams, S. J. Stranick, E. Garratt, I. Kalish, A. V. Davydov, R. K. Kanjolia and J. E. Maslar, *Chem. Mater.*, 2017, **29**, 6279–6288.

23 Z. Fang, L. Peng, Y. Qian, X. Zhang, Y. Xie, J. J. Cha and G. Yu, *J. Am. Chem. Soc.*, 2018, **140**, 5241–5247.

24 K. A. Sree Raj, N. Barman, S. Radhakrishnan, R. Thapa and C. S. Rout, *J. Mater. Chem. A*, 2022, **10**, 23590–23602.

25 B. You and Y. Sun, *Adv. Energy Mater.*, 2016, **6**, 1502333.

26 W. Cao, W. Zhao, C. Xiong, Q. Long, N. Chen and G. Du, *J. Energy Storage*, 2023, **64**, 107213.

27 E. Hu, J. Ning, D. Zhao, C. Xu, Y. Lin, Y. Zhong, Z. Zhang, Y. Wang and Y. Hu, *Small*, 2018, **14**, 1704233.

28 H. Tabassum, W. Guo, W. Meng, A. Mahmood, R. Zhao, Q. Wang and R. Zou, *Adv. Energy Mater.*, 2017, **7**, 1601671.

29 D. Spurling, H. Krüger, N. Kohlmann, F. Rasch, M. P. Kremer, L. Kienle, R. Adelung, V. Nicolosi and F. Schütt, *Energy Storage Mater.*, 2024, **65**, 103148.

30 D. Sun, L. Ye, F. Sun, H. Garcia and Z. Li, *Inorg. Chem.*, 2017, **56**, 5203–5209.

31 J. Yang, J. Wang, H. Li, Z. Wu, Y. Xing, Y. Chen and L. Liu, *Adv. Sci.*, 2022, **9**, 2101988.

32 Y. P. Zhu, T. Y. Ma, M. Jaroniec and S. Z. Qiao, *Angew. Chem., Int. Ed.*, 2017, **56**, 1324–1328.

33 H. Zhang, J. Nai, L. Yu and X. W. D. Lou, *Joule*, 2017, **1**, 77–107.

34 Z. Zheng, L. Lin, S. Mo, D. Ou, J. Tao, R. Qin, X. Fang and N. Zheng, *Small*, 2018, **14**, 1800759.

35 Y. Von Lim, S. Huang, Y. Zhang, D. Kong, Y. Wang, L. Guo, J. Zhang, Y. Shi, T. P. Chen and L. K. Ang, *Energy Storage Mater.*, 2018, **15**, 98–107.

36 X. Wang, Q. Li, N. Yang, Y. Yang, F. He, J. Chu, M. Gong, B. Wu, R. Zhang and S. Xiong, *J. Solid State Chem.*, 2019, **270**, 370–378.

37 F. Zou, Y.-M. Chen, K. Liu, Z. Yu, W. Liang, S. M. Bhaway, M. Gao and Y. Zhu, *ACS Nano*, 2016, **10**, 377–386.

38 Y. Tang, W. Guo and R. Zou, *Coord. Chem. Rev.*, 2022, **451**, 214242.

39 Z. Chang, X. Ju, P. Guo, X. Zhu and X. Zheng, *J. Alloys Compd.*, 2020, **824**, 153873.

40 X. Wang, J. Feng, Y. Bai, Q. Zhang and Y. Yin, *Chem. Rev.*, 2016, **116**, 10983–11060.

41 E. Miele, S. Raj, Z. Baraissov, P. Král and U. Mirsaidov, *Adv. Mater.*, 2017, **29**, 1702682.

42 F. He, G. Chen, J. Miao, Z. Wang, D. Su, S. Liu, W. Cai, L. Zhang, S. Hao and B. Liu, *ACS Energy Lett.*, 2016, **1**, 969–975.

43 X. Y. Yu, L. Yu and X. W. Lou, *Adv. Energy Mater.*, 2016, **6**, 1501333.

44 A. J. Howarth, Y. Liu, P. Li, Z. Li, T. C. Wang, J. T. Hupp and O. K. Farha, *Nat. Rev. Mater.*, 2016, **1**, 1–15.

45 Y. Fang, B. D. Lindner, I. Destoop, T. Tsuji, Z. Zhang, R. Z. Khaliullin, D. F. Perepichka, K. Tahara, S. D. Feyter and Y. Tobe, *J. Am. Chem. Soc.*, 2020, **142**, 8662–8671.

46 W. Wang, H. Yan, U. Anand and U. Mirsaidov, *J. Am. Chem. Soc.*, 2021, **143**, 1854–1862.

47 C. Cheng, C. Wei, Y. He, L. Liu, J. Hu and W. Du, *J. Energy Storage*, 2021, **33**, 102105.

48 S. Niu, W. J. Jiang, T. Tang, Y. Zhang, J. H. Li and J. S. Hu, *Adv. Sci.*, 2017, **4**, 1700084.

49 D. Zheng, X. Sun, C. An, F. Pan, C. Qin, Z. Wang, Q. Deng, Y. Song and Y. Li, *Chem. Eng. J.*, 2023, **473**, 145289.

50 J. M. Seco, E. San Sebastian, J. Cepeda, B. Biel, A. Salinas-Castillo, B. Fernandez, D. P. Morales, M. Bobinger, S. Gomez-Ruiz, F. C. Loghin, A. Rivadeneyra and A. Rodriguez-Dieguez, *Sci. Rep.*, 2018, **8**, 14414.

51 L. Hu, X. M. Lin, J. T. Mo, J. Lin, H. L. Gan, X. L. Yang and Y. P. Cai, *Inorg. Chem.*, 2017, **56**, 4289–4295.

52 X.-H. Chen, Q. Wei, J.-D. Hong, R. Xu and T.-H. Zhou, *Rare Met.*, 2019, **38**, 413–419.

53 T. Liu, F. Zhang, Y. Song and Y. Li, *J. Mater. Chem. A*, 2017, **5**, 17705–17733.

54 J. Zheng, C. Qin, C. Chen, C. Zhang, P. Shi, X. Chen, Y. Gan, J. Li, J. Yao and X. Liu, *J. Mater. Chem. A*, 2023, **11**, 24311–24320.

55 M. Schieder, C. Bojer, J. Vom Stein, S. Koch, T. Martin, H. Schmalz, J. Breu and T. Lunkenbein, *Angew. Chem., Int. Ed.*, 2017, **129**, 14156–14160.

56 T. Kondo, Y. Kodama, S. Ikezoe, K. Yajima, T. Aikawa and M. Yuasa, *Carbon*, 2014, **77**, 783–789.

57 X. Song, Y. Jiang, F. Cheng, J. Earnshaw, J. Na, X. Li and Y. Yamauchi, *Small*, 2021, **17**, 2004142.

58 C. Bie, J. Pei, G. Chen, Q. Zhang, J. Sun, Y. Yu and D. Chen, *J. Mater. Chem. A*, 2016, **4**, 17063–17072.

59 S. Wang, J. Teng, Y. Xie, Z.-W. Wei, Y. Fan, J.-J. Jiang, H.-P. Wang, H. Liu, D. Wang and C.-Y. Su, *J. Mater. Chem. A*, 2019, **7**, 4036–4046.

60 N. Hedayat, Y. Du and H. Ilkhani, *Renewable Sustainable Energy Rev.*, 2017, **77**, 1221–1239.

61 H. Lin, Z. Zhang, Y. Wang, X. L. Zhang, Z. Tie and Z. Jin, *Adv. Funct. Mater.*, 2021, **31**, 2102735.

62 M. Kim, R. Xin, J. Earnshaw, J. Tang, J. P. Hill, A. Ashok, A. K. Nanjundan, J. Kim, C. Young and Y. Sugahara, *Nat. Protoc.*, 2022, **17**, 2990–3027.

63 J. Huang, C. Liu, Y. Jin and J. Chen, *Chem. Eng. J.*, 2023, **461**, 141930.

64 N. D. Petkovich and A. Stein, *Chem. Soc. Rev.*, 2013, **42**, 3721–3739.

65 T. Meng, L. Zheng, J. Qin, D. Zhao and M. Cao, *J. Mater. Chem. A*, 2017, **5**, 20228–20238.

66 C. Hu and L. Dai, *Adv. Mater.*, 2017, **29**, 1604942.

67 K. B. Tom, S. Lin, L. F. Wan, J. Wang, N. Ahlm, A. T. N'Diaye, K. Bustillo, J. Huang, Y. Liu and S. Lou, *ACS Nano*, 2018, **12**, 7554–7561.

68 J.-X. Feng, J.-Q. Wu, Y.-X. Tong and G.-R. Li, *J. Am. Chem. Soc.*, 2018, **140**, 610–617.

69 X. Teng, J. Wang, L. Ji, W. Tang and Z. Chen, *ACS Sustainable Chem. Eng.*, 2018, **6**, 2069–2077.

70 J. Li, J. Xu, Z. Xie, X. Gao, J. Zhou, Y. Xiong, C. Chen, J. Zhang and Z. Liu, *Adv. Mater.*, 2018, **30**, 1800548.

71 Y. Yi, L. Yu, Z. Tian, Y. Song, Y. Shao, L. Gao, J. Sun and Z. Liu, *Adv. Funct. Mater.*, 2018, **28**, 1805510.

72 K. Li, Y. Xiao, T. Zheng, Q. Sun, Y. Zhang, H. Teng, W. Wang, K. Yao, J. Rao and Y. Zhang, *Appl. Surf. Sci.*, 2023, **622**, 156950.

73 K. Li, Z. Guo, Q. Sun, X. Dai, Y. Li, K. Yao, X. Liu, Z. Bao, J. Rao and Y. Zhang, *Chem. Eng. J.*, 2023, **454**, 140223.

74 Y. Du, G. Li, M. Chen, X. Yang, L. Ye, X. Liu and L. Zhao, *Chem. Eng. J.*, 2019, **378**, 122210.

75 W. Wang, H. Yan, U. Anand and U. Mirsaidov, *J. Am. Chem. Soc.*, 2021, **143**, 1854–1862.

76 Q. Li, Z. Ren, Y. Liu, C. Zhang, J. Liu, R. Zhou, Y. Bu, F. Mao and H. Wu, *Chem. Eng. J.*, 2023, **452**, 139545.

77 Y. Li, Y. Fu, S. Chen, Z. Huang, L. Wang and Y. Song, *Composites, Part B*, 2019, **171**, 130–137.

78 H. Cheng, G. Xu, C. Zhu, Z. Alhalili, X. Du and G. Gao, *Chem. Eng. J.*, 2023, **454**, 140454.

79 P. Li, J. Ren, C. Li, J. Li, K. Zhang, T. Wu, B. Li and L. Wang, *Chem. Eng. J.*, 2023, **451**, 138536.

80 L. Shi, D. Benetti, Q. Wei and F. Rosei, *Small*, 2023, **19**, e2300606.

81 Y. Yang, L. Li, G. Ruan, H. Fei, C. Xiang, X. Fan and J. M. Tour, *ACS Nano*, 2014, **8**, 9622–9628.

82 P. Xie, W. Yuan, X. Liu, Y. Peng, Y. Yin, Y. Li and Z. Wu, *Energy Storage Mater.*, 2021, **36**, 56–76.

83 J. Zhang, Y. Song, M. Kopeć, J. Lee, Z. Wang, S. Liu, J. Yan, R. Yuan, T. Kowalewski and M. R. Bockstaller, *J. Am. Chem. Soc.*, 2017, **139**, 12931–12934.

84 B. You, Y. Zhang, P. Yin, D.-e. Jiang and Y. Sun, *Nano Energy*, 2018, **48**, 600–606.

85 D. Yan, L. Liu, X. Wang, K. Xu and J. Zhong, *Chem. Eng. Technol.*, 2022, **45**, 649–657.

86 J.-T. Ren, Y.-S. Wang, L. Chen, L.-J. Gao, W.-W. Tian and Z.-Y. Yuan, *Chem. Eng. J.*, 2020, **389**, 124408.

87 Y.-P. Zhu, X. Xu, H. Su, Y.-P. Liu, T. Chen and Z.-Y. Yuan, *ACS Appl. Mater. Interfaces*, 2015, **7**, 28369–28376.

88 X. Lv, W. Tian, Y. Liu and Z.-Y. Yuan, *Mater. Chem. Front.*, 2019, **3**, 2428–2436.

89 J. Yang, X. Wang, B. Li, L. Ma, L. Shi, Y. Xiong and H. Xu, *Adv. Funct. Mater.*, 2017, **27**, 1606497.

90 P. Jia, H. Yao, Q. Liu, J. Wang, Z. Li and L. Zhang, *J. Alloys Compd.*, 2023, **958**, 170525.

91 A. Kumar and S. Bhattacharyya, *ACS Appl. Mater. Interfaces*, 2017, **9**, 41906–41915.

92 Q. Yuan, Y. Yu, Y. Gong and X. Bi, *ACS Appl. Mater. Interfaces*, 2019, **12**, 3592–3602.

93 H. Zhang, X. Liu, Y. Wu, C. Guan, A. K. Cheetham and J. Wang, *Chem. Commun.*, 2018, **54**, 5268–5288.

94 K. Li, H. Teng, Q. Sun, Y. Li, X. Wu, X. Dai, Y. Wang, S. Wang, Y. Zhang and K. Yao, *J. Energy Storage*, 2022, **53**, 105094.

95 T. Y. Ma, S. Dai, M. Jaroniec and S. Z. Qiao, *J. Am. Chem. Soc.*, 2014, **136**, 13925–13931.

96 X. Ma, W. Zhang, Y. Deng, C. Zhong, W. Hu and X. Han, *Nanoscale*, 2018, **10**, 4816–4824.

97 X.-W. Lv, Y. Liu, W. Tian, L. Gao and Z.-Y. Yuan, *J. Energy Chem.*, 2020, **50**, 324–331.

98 Z. Wang, H. Liu, R. Ge, X. Ren, J. Ren, D. Yang, L. Zhang and X. Sun, *ACS Catal.*, 2018, **8**, 2236–2241.

99 K. Li, S. Feng, C. Jing, Y. Chen, X. Liu, Y. Zhang and L. Zhou, *Chem. Commun.*, 2019, **55**, 13773–13776.

100 K. Li, X. Liu, T. Zheng, D. Jiang, Z. Zhou, C. Liu, X. Zhang, Y. Zhang and D. Losic, *Chem. Eng. J.*, 2019, **370**, 136–147.

101 A. Wu, Y. Xie, H. Ma, C. Tian, Y. Gu, H. Yan, X. Zhang, G. Yang and H. Fu, *Nano Energy*, 2018, **44**, 353–363.

102 H. Zhang, X. Li, A. Hähnel, V. Naumann, C. Lin, S. Azimi, S. L. Schweizer, A. W. Maijenburg and R. B. Wehrspohn, *Adv. Funct. Mater.*, 2018, **28**, 1706847.

103 K. N. Dinh, P. Zheng, Z. Dai, Y. Zhang, R. Dangol, Y. Zheng, B. Li, Y. Zong and Q. Yan, *Small*, 2018, **14**, 1703257.

104 Z. Wu, X. Wang, J. Huang and F. Gao, *J. Mater. Chem. A*, 2018, **6**, 167–178.

105 L. Sun, G. Yuan, L. Gao, J. Yang, M. Chhowalla, M. H. Gharahcheshmeh, K. K. Gleason, Y. S. Choi, B. H. Hong and Z. Liu, *Nat. Rev. Methods Primers*, 2021, **1**, 5.

106 F. Liu, P. Li, H. An, P. Peng, B. McLean and F. Ding, *Adv. Funct. Mater.*, 2022, **32**, 2203191.

107 A. Cohen, A. Patsha, P. K. Mohapatra, M. Kazes and A. Ismach, *ACS Nano*, 2020, **17**, 5399–5411.

108 C. E. Reilly, S. Keller, S. Nakamura and S. P. DenBaars, *Light: Sci. Appl.*, 2021, **10**, 150.

109 S. H. Choi, B. Stephen, J.-H. Park, J. S. Lee, S. M. Kim, W. Yang and K. K. Kim, *Sci. Rep.*, 2017, **7**, 1983.

110 S. Cwik, D. Mitoraj, O. Mendoza Reyes, D. Rogalla, D. Peeters, J. Kim, H. M. Schütz, C. Bock, R. Beranek and A. Devi, *Adv. Mater. Interfaces*, 2018, **5**, 1800140.

111 J. Lv, T. Liang, M. Yang, S. Ken and M. Hideo, *J. Energy Chem.*, 2017, **26**, 330–335.

112 K. Li, Z. Hu, R. Zhao, J. Zhou, C. Jing, Q. Sun, J. Rao, K. Yao, B. Dong and X. Liu, *J. Colloid Interface Sci.*, 2021, **603**, 799–809.

113 M. E. Warwick, A. J. Roberts, R. C. Slade and R. Binions, *J. Mater. Chem. A*, 2014, **2**, 6115–6120.

114 H. Kim, S. Oh, E. Cho and H. Kwon, *ACS Sustainable Chem. Eng.*, 2018, **6**, 6305–6311.

115 L. Yang and L. Zhang, *Appl. Catal., B*, 2019, **259**, 118053.

116 Y. P. Zhu, Y. P. Liu, T. Z. Ren and Z. Y. Yuan, *Adv. Funct. Mater.*, 2015, **25**, 7337–7347.

117 K. Liang, L. Guo, K. Marcus, S. Zhang, Z. Yang, D. E. Perea, L. Zhou, Y. Du and Y. Yang, *ACS Catal.*, 2017, **7**, 8406–8412.

118 K. Xiao, L. Zhou, M. Shao and M. Wei, *J. Mater. Chem. A*, 2018, **6**, 7585–7591.

119 Y. Pei, Y. Yang, F. Zhang, P. Dong, R. Baines, Y. Ge, H. Chu, P. M. Ajayan, J. Shen and M. Ye, *ACS Appl. Mater. Interfaces*, 2017, **9**, 31887–31896.

120 Z. Lei, J. Bai, Y. Li, Z. Wang and C. Zhao, *ACS Appl. Mater. Interfaces*, 2017, **9**, 35837–35846.

121 L. Yu, H. Zhou, J. Sun, F. Qin, F. Yu, J. Bao, Y. Yu, S. Chen and Z. Ren, *Energy Environ. Sci.*, 2017, **10**, 1820–1827.

122 H. Liu, X. Liu, S. Wang, H.-K. Liu and L. Li, *Energy Storage Mater.*, 2020, **28**, 122–145.

123 R. Liu, A. Zhou, X. Zhang, J. Mu, H. Che, Y. Wang, T.-T. Wang, Z. Zhang and Z. Kou, *Chem. Eng. J.*, 2021, **412**, 128611.

124 G. Tatrari, M. Ahmed and F. U. Shah, *Coord. Chem. Rev.*, 2024, **498**, 215470.

125 Y. Wang, S. Sun, X. Wu, H. Liang and W. Zhang, *Nano-Micro Lett.*, 2023, **15**, 78.

126 Y. Wang, J. Sun, S. Li, Y. Zhang, C. Xu and H. Chen, *J. Alloys Compd.*, 2020, **824**, 153939.

127 H. Chen, J. Wang, F. Liao, X. Han, C. Xu and Y. Zhang, *Ceram. Int.*, 2019, **45**, 8008–8016.

128 Y. Zhang, S. Yu, G. Lou, Y. Shen, H. Chen, Z. Shen, S. Zhao, J. Zhang, S. Chai and Q. Zou, *J. Mater. Sci.*, 2017, **52**, 11201–11228.

129 L. Eliad, G. Salitra, A. Soffer and D. Aurbach, *J. Phys. Chem. B*, 2001, **105**, 6880–6887.

130 X. Li, L. Jiang, C. Zhou, J. Liu and H. Zeng, *NPG Asia Mater.*, 2015, **7**, e165.

131 S. Zhang, K. Wang, H. Chen, H. Liu, L. Yang, Y. Chen and H. Li, *Carbon*, 2022, **194**, 10–22.

132 X. Yan, X. Wang, Y. Dai, Y. He, Z. Cai, Y. Wang and X. Wang, *J. Mater. Sci.: Mater. Electron.*, 2019, **30**, 17218–17226.

133 Q. Jiang, Y. Lei, H. Liang, K. Xi, C. Xia and H. N. Alshareef, *Energy Storage Mater.*, 2020, **27**, 78–95.

134 M. Gao, F. Wang, S. Yang, A. G. Ricciardulli, F. Yu, J. Li, J. Sun, R. Wang, Y. Huang and P. Zhang, *Mater. Today*, 2023.

135 K. Nasrin, V. Sudharshan, K. Subramani and M. Sathish, *Adv. Funct. Mater.*, 2022, **32**, 2110267.

136 Z. Liu, Z. Zhao, W. Zhang, Y. Huang, Y. Liu, D. Wu, L. Wang and S. Chou, *InfoMat*, 2022, **4**, e12260.

137 Y. Boyjoo, M. Wang, V. K. Pareek, J. Liu and M. Jaroniec, *Chem. Soc. Rev.*, 2016, **45**, 6013–6047.

138 S. Aloqayli, C. Ranaweera, Z. Wang, K. Siam, P. Kahol, P. Tripathi, O. Srivastava, B. K. Gupta, S. Mishra and F. Perez, *Energy Storage Mater.*, 2017, **8**, 68–76.

139 X. Yang, K. Xu, R. Zou and J. Hu, *Nano-Micro Lett.*, 2016, **8**, 143–150.

140 X. Wu, L. Meng, Q. Wang, W. Zhang and Y. Wang, *Chem. Eng. J.*, 2017, **327**, 193–201.

141 J. Jiang, W. Shi, S. Song, Q. Hao, W. Fan, X. Xia, X. Zhang, Q. Wang and D. Yan, *J. Power Sources*, 2014, **248**, 1281–1289.

142 Y. Zhao, X. Wang, H. Li, B. Qian, Y. Zhang and Y. Wu, *Chem. Eng. J.*, 2022, **431**, 133981.

143 M. Pal, R. Rakshit, A. K. Singh and K. Mandal, *Energy*, 2016, **103**, 481–486.

144 F. Liu, H. Su, L. Jin, H. Zhang, X. Chu and W. Yang, *J. Colloid Interface Sci.*, 2017, **505**, 796–804.

145 T. Yao, X. Guo, S. Qin, F. Xia, Q. Li, Y. Li, Q. Chen, J. Li and D. He, *Nano-Micro Lett.*, 2017, **9**, 1–8.

146 M. M. Sk, C. Y. Yue, K. Ghosh and R. K. Jena, *J. Power Sources*, 2016, **308**, 121–140.

147 D.-S. Kong, J.-M. Wang, H.-B. Shao, J.-Q. Zhang and C.-n. Cao, *J. Alloys Compd.*, 2011, **509**, 5611–5616.

148 L. Wang, H. Yang, X. Liu, R. Zeng, M. Li, Y. Huang and X. Hu, *Angew. Chem., Int. Ed.*, 2017, **56**, 1105–1110.

149 Y. Li, J. Xu, T. Feng, Q. Yao, J. Xie and H. Xia, *Adv. Funct. Mater.*, 2017, **27**, 1606728.

150 Q. Yang, Z. Lu, X. Sun and J. Liu, *Sci. Rep.*, 2013, **3**, 3537.

151 W. Feng, V. S. Avvaru, S. J. Hinder and V. Etacheri, *J. Energy Chem.*, 2022, **69**, 338–346.

152 G. Meng, Q. Yang, X. Wu, P. Wan, Y. Li, X. Lei, X. Sun and J. Liu, *Nano energy*, 2016, **30**, 831–839.

153 S. Liu, S. C. Lee, U. M. Patil, C. Ray, K. V. Sankar, K. Zhang, A. Kundu, J. H. Park and S. C. Jun, *J. Mater. Chem. A*, 2017, **5**, 4543–4549.

154 J. Lin, H. Jia, H. Liang, S. Chen, Y. Cai, J. Qi, C. Qu, J. Cao, W. Fei and J. Feng, *Adv. Sci.*, 2018, **5**, 1700687.

155 R. Wang, S. Cai, Y. Yan, W. M. Yourey, W. Tong and H. Tang, *J. Mater. Chem. A*, 2017, **5**, 22648–22653.

156 A. Zhang, R. Zhao, L. Hu, R. Yang, S. Yao, S. Wang, Z. Yang and Y. M. Yan, *Adv. Energy Mater.*, 2021, **11**, 2101412.

157 Y. Zhou, X. Cheng, B. Tynan, Z. Sha, F. Huang, M. S. Islam, J. Zhang, A. N. Rider, L. Dai and D. Chu, *Carbon*, 2021, **184**, 504–513.

158 M. Qiu, P. Sun, L. Shen, K. Wang, S. Song, X. Yu, S. Tan, C. Zhao and W. Mai, *J. Mater. Chem. A*, 2016, **4**, 7266–7273.

159 R. Velmurugan, P. Alagammai, M. Ulaganathan and B. Subramanian, *J. Mater. Chem. A*, 2020, **8**, 24148–24165.

160 M. Kundu, D. Mondal, I. Mondal, A. Baral, P. Halder, S. Biswas, B. Paul, N. Bose, R. Basu and S. Das, *J. Energy Chem.*, 2023, **87**, 192–206.

161 S. Liu, C. Xu, H. Yang, G. Qian, S. Hua, J. Liu, X. Zheng and X. Lu, *Small*, 2020, **16**, 1905778.

162 M. Qorbani, O. Khajehdehi, A. Sabbah and N. Naseri, *ChemSusChem*, 2019, **12**, 4064–4073.

163 Z. Shao, H. Li, M. Li, C. Li, C. Qu and B. Yang, *Energy*, 2015, **87**, 578–585.

164 J. Kang, A. Hirata, L. Kang, X. Zhang, Y. Hou, L. Chen, C. Li, T. Fujita, K. Akagi and M. Chen, *Angew. Chem., Int. Ed.*, 2013, **52**, 1664–1667.

165 Y. Liu, N. Fu, G. Zhang, M. Xu, W. Lu, L. Zhou and H. Huang, *Adv. Funct. Mater.*, 2017, **27**, 1605307.

166 H. Arandiyan, Y. Wang, H. Sun, M. Rezaei and H. Dai, *Chem. Commun.*, 2018, **54**, 6484–6502.

167 X. Liu, G. Du, J. Zhu, Z. Zeng and X. Zhu, *Appl. Surf. Sci.*, 2016, **384**, 92–98.

168 M. S. Chavali and M. P. Nikolova, *SN Appl. Sci.*, 2019, **1**.

169 S. Rezaee and S. Shahrokhian, *Appl. Catal., B*, 2019, **244**, 802–813.

170 R. Wu, X. Qian, A. W.-K. Law and K. Zhou, *RSC Adv.*, 2016, **6**, 50846–50850.

171 L. Pan, T. Muhammad, L. Ma, Z.-F. Huang, S. Wang, L. Wang, J.-J. Zou and X. Zhang, *Appl. Catal., B*, 2016, **189**, 181–191.

172 C. Guan, A. Sumboja, H. Wu, W. Ren, X. Liu, H. Zhang, Z. Liu, C. Cheng, S. J. Pennycook and J. Wang, *Adv. Mater.*, 2017, **29**, 1704117.

173 S. S. Mofarah, E. Adabifiroozjaei, Y. Wang, H. Arandiyan, R. Pardehkhorram, Y. Yao, M. H. N. Assadi, R. Mehmood, W.-F. Chen and C. Tsounis, *J. Mater. Chem. A*, 2020, **8**, 4753–4763.

174 H. Y. Yuan, P. F. Liu and H. G. Yang, *Matter*, 2022, **5**, 1063–1065.

175 Y. Ou, L. P. Twight, B. Samanta, L. Liu, S. Biswas, J. L. Fehrs, N. A. Sagui, J. Villalobos, J. Morales-Santelices and D. Antipin, *Nat. Commun.*, 2023, **14**, 7688.

176 R. Patel, J. T. Park, M. Patel, J. K. Dash, E. B. Gowd, R. Karpoormath, A. Mishra, J. Kwak and J. H. Kim, *J. Mater. Chem. A*, 2018, **6**, 12–29.

177 H. Wang, H. S. Casalongue, Y. Liang and H. Dai, *J. Am. Chem. Soc.*, 2010, **132**, 7472–7477.

178 L. Gao, K. Cao, H. Zhang, P. Li, J. Song, J. U. Surjadi, Y. Li, D. Sun and Y. Lu, *J. Mater. Chem. A*, 2017, **5**, 16944–16952.

179 M. Gao, M. Li, J. Yang, Y. Liu, Y. Liu, X. Zhang, S. Wu and K. Cai, *Chem. Eng. J.*, 2022, **429**, 132423.

180 Q. Wang and D. O'Hare, *Chem. Rev.*, 2012, **112**, 4124–4155.

181 L. Brooks, *J. Am. Chem. Soc.*, 1952, **74**, 227–229.

182 S. Li, P. Cheng, J. Luo, D. Zhou, W. Xu, J. Li, R. Li and D. Yuan, *Nano-Micro Lett.*, 2017, **9**, 1–10.

183 W. Gu, L. Hu, W. Hong, X. Jia, J. Li and E. Wang, *Chem. Sci.*, 2016, **7**, 4167–4173.

184 Q. Song, Z. Wu, Y. X. Wang, S. X. Dou and J. Yang, *Adv. Energy Mater.*, 2023, 2300739.

185 X. Han, K. Tao, D. Wang and L. Han, *Nanoscale*, 2018, **10**, 2735–2741.

186 W. Chen, T. Wei, L.-E. Mo, S. Wu, Z. Li, S. Chen, X. Zhang and L. Hu, *Chem. Eng. J.*, 2020, **400**, 125856.

187 P. Cai, J. Huang, J. Chen and Z. Wen, *Angew. Chem., Int. Ed.*, 2017, **129**, 4936–4939.

188 H. Wang, M. Liang, H. Ma, H. Zhang, Z. Guo, Y. Zhao, Y. Zhao, N. ur RehmanLashari and Z. Miao, *J. Energy Storage*, 2023, **58**, 106322.

189 J. Chen, W. R. Walker, L. Xu, O. Krysiak, Z. She and M. A. Pope, *ACS Nano*, 2020, **14**, 5636–5648.

190 Y. M. Chen, X. Y. Yu, Z. Li, U. Paik and X. W. Lou, *Sci. Adv.*, 2016, **2**, e1600021.

191 X. Y. Yu and X. W. Lou, *Adv. Energy Mater.*, 2018, **8**, 1701592.

192 A. Mohammadi, S. E. Moosavifard, A. Goljanian Tabrizi, M. M. Abdi and G. Karimi, *ACS Appl. Energy Mater.*, 2018, **2**, 627–635.

193 L. Chen, L. Han, X. Liu, Y. Li and M. Wei, *Chemistry*, 2021, **27**, 2104–2111.

194 J. Xu, J. Li, D. Xiong, B. Zhang, Y. Liu, K.-H. Wu, I. Amorim, W. Li and L. Liu, *Chem. Sci.*, 2018, **9**, 3470–3476.

195 R. Zhang, P. A. Russo, M. Feist, P. Amsalem, N. Koch and N. Pinna, *ACS Appl. Mater. Interfaces*, 2017, **9**, 14013–14022.

196 H. Wan, L. Li, Y. Chen, J. Gong, M. Duan, C. Liu, J. Zhang and H. Wang, *Electrochim. Acta*, 2017, **229**, 380–386.

197 S. Liu, K. V. Sankar, A. Kundu, M. Ma, J.-Y. Kwon and S. C. Jun, *ACS Appl. Mater. Interfaces*, 2017, **9**, 21829–21838.

198 P. A. K. Reddy, H. Han, K. C. Kim and S. Bae, *Chem. Eng. J.*, 2023, **471**, 144608.

199 L. Cao, S. Yang, W. Gao, Z. Liu, Y. Gong, L. Ma, G. Shi, S. Lei, Y. Zhang and S. Zhang, *Small*, 2013, **9**, 2905–2910.

200 S. S. Nardekar, K. Krishnamoorthy, P. Pazhamalai, S. Sahoo, V. K. Mariappan and S.-J. Kim, *J. Mater. Chem. A*, 2020, **8**, 13121–13131.

201 X. Jian, H. Li, H. Li, Y. Li and Y. Shang, *Carbon*, 2021, **172**, 132–137.

202 T. Sun, Z. Li, X. Liu, L. Ma, J. Wang and S. Yang, *J. Power Sources*, 2017, **352**, 135–142.

203 Q. Wang, F. Gao, B. Xu, F. Cai, F. Zhan, F. Gao and Q. Wang, *Chem. Eng. J.*, 2017, **327**, 387–396.

204 X. Cao, J. He, H. Li, L. Kang, X. He, J. Sun, R. Jiang, H. Xu, Z. Lei and Z. H. Liu, *Small*, 2018, **14**, 1800998.

205 S. Patil, J. Kim and D. Lee, *Chem. Eng. J.*, 2017, **322**, 498–509.

206 Y. Wen, S. Peng, Z. Wang, J. Hao, T. Qin, S. Lu, J. Zhang, D. He, X. Fan and G. Cao, *J. Mater. Chem. A*, 2017, **5**, 7144–7152.

207 L. Kang, C. Huang, J. Zhang, M. Zhang, N. Zhang, S. Liu, Y. Ye, C. Luo, Z. Gong and C. Wang, *Chem. Eng. J.*, 2020, **390**, 124643.

208 B. Li, Y. Shi, K. Huang, M. Zhao, J. Qiu, H. Xue and H. Pang, *Small*, 2018, **14**, 1703811.

209 M. Pramanik, S. Tominaka, Z. L. Wang, T. Takei and Y. Yamauchi, *Angew. Chem., Int. Ed.*, 2017, **129**, 13693–13697.

210 G. Xia, J. Su, M. Li, P. Jiang, Y. Yang and Q. Chen, *J. Mater. Chem. A*, 2017, **5**, 10321–10327.

211 Z. Li and L. Yin, *Energy Storage Mater.*, 2018, **14**, 367–375.

212 Z.-J. Cao, X. Dong, T. Fu, S.-B. Deng, W. Liao and Y.-Z. Wang, *Polym. Degrad. Stab.*, 2017, **136**, 103–111.

213 L. Song and S. Zhang, *Powder Technol.*, 2011, **208**, 713–716.

214 S. Kavian, S. Hajati and M. Moradi, *J. Mater. Sci.: Mater. Electron.*, 2021, **32**, 13117–13128.

215 Q. Yang, R. Zhang, W. Wang, P. Zhou, L. Wang, T. Chen, H. Xu and L. Zheng, *Sustainable Energy Fuels*, 2019, **3**, 3078–3084.

216 J. Zhu, Y. Yao, Z. Chen, A. Zhang, M. Zhou, J. Guo, W. D. Wu, X. D. Chen, Y. Li and Z. Wu, *ACS Appl. Mater. Interfaces*, 2018, **10**, 18761–18770.

217 V. M. H. Ng, H. Huang, K. Zhou, P. S. Lee, W. Que, J. Z. Xu and L. B. Kong, *J. Mater. Chem. A*, 2017, **5**, 3039–3068.

218 K. Zhang, G. Zhang, J. Qu and H. Liu, *ACS Appl. Mater. Interfaces*, 2018, **10**, 2451–2459.

219 X. Xu, F. Nosheen and X. Wang, *Chem. Mater.*, 2016, **28**, 6313–6320.

220 Q. Wan, S. Li and J.-B. Liu, *ACS Appl. Mater. Interfaces*, 2018, **10**, 6369–6377.

221 Y. Zhao, M. Zhao, X. Ding, Z. Liu, H. Tian, H. Shen, X. Zu, S. Li and L. Qiao, *Chem. Eng. J.*, 2019, **373**, 1132–1143.

222 L. Sun, Z. Xie, A. Wu, C. Tian, D. Wang, Y. Gu, Y. Gao and H. Fu, *J. Mater. Chem. A*, 2021, **9**, 26226–26235.

223 X. Wei, Y. Song, L. Song, X. D. Liu, Y. Li, S. Yao, P. Xiao and Y. Zhang, *Small*, 2021, **17**, 2007062.

224 Z. Wang, Y. Gan, Y. Wang, L. Lv, H. Wan and H. Wang, *J. Energy Storage*, 2022, **55**, 105378.

225 X. Chen, M. Cheng, D. Chen and R. Wang, *ACS Appl. Mater. Interfaces*, 2016, **8**, 3892–3900.

226 Y. Jin, C. Zhao, Q. Jiang and C. Ji, *Appl. Surf. Sci.*, 2018, **450**, 170–179.

227 J. Xu, N. Yang, S. Heuser, S. Yu, A. Schulte, H. Schönherr and X. Jiang, *Adv. Energy Mater.*, 2019, **9**, 1803623.

228 H. Foratirad, M. Maragheh and H. Baharvandi, *Rare Met.*, 2022, **41**, 3220–3227.

229 H. Vrubel and X. Hu, *Angew. Chem., Int. Ed. Engl.*, 2012, **51**, 12703–12706.

230 X. Jia, M. Wang, G. Liu, Y. Wang, J. Yang and J. Li, *Int. J. Hydrogen Energy*, 2019, **44**, 24572–24579.

231 A. Kong, Q. Lin, C. Mao, X. Bu and P. Feng, *Chem. Commun.*, 2014, **50**, 15619–15622.

232 A. M. Mohamed, S. A. Shaban, H. A. El Sayed, B. E. Alanadouli and N. K. Allam, *Int. J. Hydrogen Energy*, 2016, **41**, 866–872.

233 J. Theerthagiri, K. Karuppasamy, G. Durai, A. U. H. S. Rana, P. Arunachalam, K. Sangeetha, P. Kuppusami and H.-S. Kim, *Nanomaterials*, 2018, **8**, 256.

234 F. Ma, J. Lu, L. Pu, W. Wang and Y. Dai, *J. Colloid Interface Sci.*, 2020, **563**, 435–446.

235 A. M. Mohamed, M. Ramadan, N. Ahmed, A. O. A. ElNaga, H. H. Alalawy, T. Zaki, S. A. Shaban, H. B. Hassan and N. K. Allam, *J. Energy Storage*, 2020, **28**, 101292.

236 J. Acharya, G. P. Ojha, B. Pant and M. Park, *J. Mater. Chem. A*, 2021, **9**, 23977–23993.

237 J. Zhou, F. Liu, J. Lin, X. Huang, J. Xia, B. Zhang, Q. Zeng, H. Wang, C. Zhu, L. Niu, X. Wang, W. Fu, P. Yu, T. R. Chang, C. H. Hsu, D. Wu, H. T. Jeng, Y. Huang, H. Lin, Z. Shen, C. Yang, L. Lu, K. Suenaga, W. Zhou, S. T. Pantelides, G. Liu and Z. Liu, *Adv. Mater.*, 2017, **29**.

238 X. Zhang, T. H. Choudhury, M. Chubarov, Y. Xiang, B. Jariwala, F. Zhang, N. Alem, G. C. Wang, J. A. Robinson and J. M. Redwing, *Nano Lett.*, 2018, **18**, 1049–1056.

239 M. Liu, Z. Wang, J. Liu, G. Wei, J. Du, Y. Li, C. An and J. Zhang, *J. Mater. Chem. A*, 2017, **5**, 1035–1042.

240 M. B. Poudel, A. R. Kim, S. Ramakrishan, N. Logeshwaran, S. K. Ramasamy, H. J. Kim and D. J. Yoo, *Composites, Part B*, 2022, **247**, 110339.

241 T. Kshetri, T. I. Singh, Y. S. Lee, D. D. Khumujam, N. H. Kim and J. H. Lee, *Composites, Part B*, 2021, **211**, 108624.